



1 **Winter mixing, mesoscale eddies and eastern boundary current: Engines for biogeochemical**
2 **variability of the central Red Sea during winter/early spring period.**

3

4 Nikolaos D. Zarokanellos¹ and Burton H. Jones¹

5

6 ¹King Abdullah University of Science and Technology (KAUST), Red Sea Research Center (RSRC),
7 Biological and Environmental Sciences & Engineering Division (BESE), Bioscience program, Thuwal,
8 23955-6900, Saudi Arabia.

9

10 Correspondence to: Nikolaos D. Zarokanellos (nikolaos.zarokanellos@kaust.edu.sa)

11

12 **Abstract**

13 The central Red Sea (CRS) has been shown to be characterized by significant eddy activity throughout
14 the year. Weakened stratification in winter may lead to enhanced vertical exchange contributing to
15 physical and biogeochemical processes. In the winter of 2014-2015, we began an extended glider time
16 series to monitor the CRS where eddy activity is significant. Remote sensing and glider observations
17 that include temperature, salinity, oxygen, carbon dissolved organic matter (CDOM), chlorophyll
18 fluorescence (CHL) and multi-wavelength optical backscatter have been used to characterize the effects
19 of winter mixing, eddy activity and lateral advection. During winter and early spring, mixing up to 90m
20 driven by surface cooling and strong winds combined with eddy features was insufficient to penetrate
21 the nutricline and supply nutrients into the upper layer. However, the mixing events did disperse the
22 phytoplankton from the deep chlorophyll maximum throughout the upper mixed layer (ML) increasing
23 the chlorophyll signature detected by ocean colour imagery. In early spring, the eastern boundary
24 current (EBC) is evident in CRS. The EBC brings relative high concentrations of CHL and CDOM
25 along with lower oxygen concentrations indicative of previous nutrient availability. In addition to the
26 vertical mixing, mesoscale eddy activity cause 160m vertical displacement of the 180 μM isopleth of
27 oxygen, proxy of the nutricline interface. Within the cyclonic feature, this oxygen isopleth shallowed to
28 60m, well within the euphotic layer. Remote sensing analyses indicate that these eddies also contribute



29 to significant horizontal dispersion, including the exchange between the open sea and coastal coral reef
30 ecosystems. When the phytoplankton is distributed through the mixed layer clear diel variability was
31 evident in CHL concentration. The biogeochemical responses provide a sensitive indicator of the
32 mixing and eddy processes that may not be detectable via remote sensing. Sustained in situ autonomous
33 observations were essential to understand these processes.

34

35 **1. Introduction**

36 The Red Sea is a narrow and long basin surrounded by hot deserts, and is isolated from the
37 world's oceans with no major connection to water bodies other than the Indian Ocean via Bab el
38 Mandeb, which is located between the Asian and African continents. The Red Sea is characterized by
39 negligible fresh water input from rainfall and terrestrial runoff, high temperatures and high salinity due
40 to large evaporation rates (Edwards, 1987; Smeed, 1997; Sofianos et al., 2002) and is a predominantly
41 oligotrophic sea (Grasshoff, 1969; Edwards, 1987). Furthermore, the Red Sea contains one of the most
42 diverse marine ecosystems in the world with important economic and environmental impacts primarily
43 due to coral reefs (Belkin, 2009; Longhurst, 2007; Raitzos et al., 2013). Coral reefs are often referred to
44 as “marine rainforests” and have concentrated in them the most diverse life in the oceans, although they
45 are fragile and vulnerable to oceanic warming (Cantin et al., 2010).

46 The wind and thermohaline forces drive the large-scale circulation of the Red Sea (Patzert,
47 1974; Phillips, 1966). Until recently, in situ observations of the Red Sea have been limited (Bower et
48 al., 2013; Morcos, 1970; Qurban et al., 2014; S.Morcos, 1974; Sofianos and Johns, 2007; Zhai, 2014;
49 Zarokanellos et al., 2017a, Zarokanellos e al., 2017b). Our knowledge regarding the variability of the
50 basin-scale circulation relied primarily on ocean models (Clifford et al., 1997; Sofianos and Johns,
51 2002, 2003; Tragou and Garrett, 1997; Yao et al., 2014a, 2014b). Numerical simulations and remote
52 sensing studies indicate that much of the time, mesoscale eddies that can propagate both zonally and
53 meridionally prevail over most of the basin (Raitzos et al., 2013; Yao et al., 2014a, 2014b; Zhan, 2013).
54 Chen et al. (2014) showed that mesoscale eddies play a significant role in the transport of heat, salt and
55 biological and chemical constituents in the Red Sea. Also, they provide valuable ecosystem services for
56 the reef system, pelagic species, and marine mammals (Shulzitski et al., 2016). Although mesoscale



57 processes seem to have a substantial effect on the Red Sea ecosystem, in situ observations to study the
58 interaction between eddies and the coastal region, and their role in the modulation of phytoplankton
59 productivity and biomass within the Red Sea remain poorly understood.

60 In the parts of oceans like the CRS where vertical exchange is limited, mesoscale features are
61 likely to play a fundamental role in controlling phytoplankton via local nutrient fluxes (Longhurst,
62 2007). The eddy activity influences both optical and biological properties in the oceans (Kheireddine et
63 al., 2017; Mahadevan, 2014; McGillicuddy et al., 1998; Pearman et al., 2017; Siegel et al., 2008).
64 Eddies also have an important impact on the vertical transport of nutrients in the upper layer of the
65 water column (Martin and Richards, 2001; McGillicuddy et al., 2003). Eddy transport affects the
66 biochemical variability of the CRS (Zarokanellos et al., 2017b). A variety of environmental forcing
67 factors can also influence the biogeochemical fluxes in the upper layer of the Red Sea, including
68 seasonal mixing, eddy interactions, and cross-shelf eddy interaction. Until now, only remote sensing
69 studies have been done to examine the seasonal variability of phytoplankton (Acker et al., 2008; Racault
70 et al., 2015; Raitzos et al., 2013). Despite the fact that remote sensing technology has enormous
71 spatiotemporal coverage to sample the surface expression of the ocean, the persistent clouds and
72 atmospheric aerosol, sun-glint, and sensor saturation over sand limit data acquisition in the Red Sea
73 (Racault et al., 2015). The Red Sea remains underexplored despite the ecological impact on several bio-
74 physical processes, including the basic circulation pattern and the water mass formation, which are still
75 obscure and highly debated (Sofianos and Johns, 2007). However, satellite imagery suggests that there
76 is an ecological connection between the coastal zone and basin. This is significant, especially for the
77 coral communities that live at the basin edge (Acker et al., 2008). The satellite imagery of surface CHL
78 often gives us evidence of the water exchange but still needed to confirm from in-situ observations.
79 Conversely, satellite remote sensing has failed to inform us regarding the vertical structure of CHL, as
80 ocean color measurements are limited to the first optical depth.

81 The Red Sea is experiencing increased anthropogenic pressure due to oil exploration,
82 aquaculture, urban and industrial development, and proposed deep-sea mining. One aspect of the
83 ecological response to the increased environment stress is the changes in the biological productivity due
84 to the stressors; it is essential to undertake the long-term monitoring of carbon cycling. Primary



85 production is not only the base for the marine food chain, but it also has a significant role in
86 biogeochemical fluxes of carbon (Green et al., 2014). Using autonomous underwater vehicles (AUVs),
87 we are able to monitor the biogeochemical properties for different spatiotemporal scales, helping us to
88 improve our knowledge and reduce uncertainties associated with carbon budgets (Cetinić et al., 2012).
89 Eddies and fronts are often enriched with nutrients in the upper layer, enhancing the primary production
90 and increasing the particle concentration (Li et al., 2012; Ohman et al., 2012; Stramma et al., 2013).
91 There are many ways to understand the interaction between the physical and bio-optical properties of
92 the Red Sea. In the past, few studies have been performed in the Red Sea, and these have primarily
93 focused on surface optical properties (Brewin et al., 2015).

94 The optical properties should covary with the CHL concentration (Siegel et al., 2005), but other
95 constituents are capable of absorbing and scattering light, such as detrital particles, CDOM, and
96 suspended solids, which all contribute independently to ocean color. The present study aims to address
97 the influence of wind mixing, eddies, fronts, and lateral advection on the optical properties.
98 Furthermore, this study examines how these physical drivers modulate the optical properties in the
99 surface and subsurface of the CRS during the winter period. Additionally, relationships between CHL,
100 CDOM, backscatter at 532nm (bbp_{532}), and particular organic carbon (POC) have been examined and
101 provide information on the primary production and optical variability in time and space. This study also
102 aims to understand the role of eddies and fronts in carbon export via both gravitational sinking and
103 subduction.

104 The present study is organized as follows: in situ and satellite observations with methods
105 described in section 2. Section 3 addresses the atmospheric forcing and the key physical dynamical
106 responses in the CRS during the winter/early spring period. It also presents the spatiotemporal
107 variability of individual measurements and their relationship, and it describes how wind winter mixing,
108 mesoscales eddies and the EBC affect key optical parameters like CHL, CDOM, bbp_{532} , and the derived
109 POC (herefor POC) during the winter period. Discussion and conclusions are provided in section 4 and
110 5, respectively.

111

112 **2. Data Sources and Methodology**



113 2.1 Glider Observations

114 Data from two Seaglider missions was obtained as part of the on-going research in the CRS (Fig
115 1a). The glider was deployed along an L-shaped transect, taking measurements for a total of 91 days
116 during the winter period from December 2, 2014 to March 2, 2015 (Fig 1b & Table 1). The 250km L-
117 shaped pattern was targeted toward to the center of a recurrent eddy that was indicated from remote
118 sensing and in situ studies (Raitsos et al. 2013; Zhan et al. 2014; Zarokanellos et al. 2017a). Each
119 deployment began offshore of the reef system Shi'b Nazar, with the glider piloted to offshore and
120 returning to the inshore end of the Yanbu line. The glider completed the round trip in about three weeks.
121 Each Seaglider measures a suite of parameters that include temperature and salinity (Sea-Bird
122 Electronics' custom CT sensor with the unpumped conductivity cell), dissolved oxygen (oxygen optode
123 4831 sensor, Aanderaa), CHL, CDOM and phycocyanin (FL3-IRB sensor, WETLAB), and the
124 customize backscatter at the following three wavelengths (532, 650 and 880; BB3 IRB sensor,
125 WETLAB). For optical backscatter we present only measurements of 532 nm, as the overall patterns for
126 650 nm and 880 nm wavelengths were very similar. Potential temperature (hereafter, pot. temperature)
127 by reference the measure temperature at depth to pressure at the surface . Both Seagliders have been
128 programmed to profile from the surface to 1000 m at the nominal vertical speed of 0.18 ± 0.02 m/s and
129 moved horizontally at approximately $20\text{-}24$ km day⁻¹. Each dive cycle took about 3-5 hours depending
130 on the operation target depth, environmental conditions, and engineering control settings. However, for
131 this study we only consider the upper 400 m layer of the water column. Spikes from the raw
132 measurements have been removed from both hydrographical and biochemical parameters. In addition,
133 CTD data has been examined for the thermal lag effect and no evidence has been observed.

134 The pre- and post-calibration activities were carried out at the Coastal and Marine Resources
135 Core Lab (CMOR) glider facility at King Abdullah University of Science and Technology (KAUST)
136 and included all ballasting, adjustment operations, and dark counts of the optical sensors necessary
137 before and after the glider deployment. In addition, a comparison was made with CTD cast from
138 hydrographical expedition in the study area, with the assumption that below 500 meters the water mass
139 changes slowly relative to the time scale of sampling such that the T-S plots from both modes of
140 sampling should tightly overlay each other (Zarokanellos et al., 2017a).



141 Evaporation rates within the Red Sea are of the order of 2 m year^{-1} (Sofianos and Johns, 2002).
 142 The high evaporation rates contribute to high salinity and significant affect the upper layer mixing (Lee
 143 et al., 2000). To estimate the mixed layer depth (MLD) we used the criteria of 0.03 kg m^{-3} where both
 144 salinity and pot. temperature are consider by using the density criterion (de Boyer Montégut, 2004). The
 145 MLD was calculated using the 1 m binned vertical profile data. CHL concentrations values based on the
 146 factory calibrations were corrected by divided that number by 2. This correction is based on comparison
 147 of fluorometer and extracted CHL measurements. The euphotic depth (Zeu) has been estimated by using
 148 the vertical profiles of CHL and defined as the depth where Photosynthetically Active Radiation (PAR)
 149 is reduced to 1% of its surface value (Morel and Maritorea, 2001). Glider fluorescence counts and
 150 optical backscatter values obtained from the WET Labs Inc. FL3 and BB3 sensors were manufactured
 151 calibrated. Raw scattering counts of optical backscatter minus dark counts were converted to total
 152 volume scattering β (124,700 nm) using a factory-calibrated scale factor. The data from sensors were
 153 converted to the engineering units by using the manufacturer calibrations:

154

$$155 [\beta(\theta_c), \text{Chla}, \text{CDOM}] = \text{scale factor} \times (\text{output} - \text{dark counts}) \quad (1)$$

156

$$157 \text{ Scale Factor} = \frac{\alpha}{(\text{output}_\alpha - \text{dark counts})} \quad (2)$$

158

$$159 \text{ Scale Factor} = E\left(\frac{b_b(532)}{\text{dark counts}}\right) \times T(\beta(\theta_c)/b_b(532)) \quad (3)$$

160

161 where scale factor (SF) from (2) and (3) is used in (1) for the computation of CHL (mg m^{-3}), CDOM
 162 (ppb) and total volume scattering at 532nm ($\beta(\theta_c)$; $\text{m}^{-1} \text{ sr}^{-1}$), respectively. In (2), the known
 163 concentration α , is the constituent of CHL or CDOM and output_α is the measured signal output for the
 164 known concentration. Furthermore, in equations (3) is the total backscattering coefficient (m^{-1}), dark
 165 counts is the signal of the sensor in the absence of light, which has been measured with a black tape
 166 over the detector, and output is the measured signal output during field sampling. In both glider
 167 missions, the optical face of the FL3 and BB3 sensor appeared clean with little to no fouling after each



168 deployment. The latter probably happened during the brief time that both gliders were in the euphotic
169 zone (<6%) and have been deployed in the most oligotrophic area of Red Sea. E and T in (3) are used
170 for denoting experimental and theoretical fractions, respectively. From $\beta(\theta_c)$, it is possible to obtain the
171 volume scattering of particles (β_p) by subtracting the volume scattering of water (β_w) (Zhang et al.,
172 2009). Then β_p is used to compute the particulate backscattering coefficients (b_{bp} ; m^{-1}) and total
173 backscattering coefficients (bb ; m^{-1}) following Boss and Pegau (Boss and Pegau, 2001). The $b_{bp}(\lambda)$ is
174 referred to simply as backscatter and can be expressed as:

175

$$176 \quad b_{bp}(532) = 2\pi\chi\beta_p(532) \quad (4)$$

177

178 Temperature and salinity correction is performed on the sensor data to obtain the more reliable values of
179 b_{bp} (Zhang et al., 2009). A detailed description of these optical computations can be found on the
180 official WETLABS website (<http://wetlabs.com/eco-puck>). Additional information about the
181 manufacturer's calibration of ECO Pucks' fluorometric measurements is found in Cetinic' et al. (2009).
182 Total volume scattering converted to particulate volume scattering coefficients, β_p , by subtracting the
183 volume scattering of seawater, β_w (Morel, 1974), and then converted to particulate backscattering b_{bp} ,
184 by a factor of $2\pi\chi$, where χ is 1.1 (Boss and Pegau, 2001). The optical backscatter at 532 nm has been
185 converted to 700 nm and then to POC concentrations using the various empirical relationships (Boss et
186 | al., 2013; Cetinić et al., 2012; Tiwari and Shanmugam, 2013).

187 Regions with high irradiance like the Red Sea tend to experience chlorophyll fluorescence
188 quenching during the daylight hours (Behrenfeld et al., 1999; Kinkade et al., 1999). The fluorescence
189 quenching during the daytime tends to occur near the surface, but this can affect the florescence in the
190 upper layer of the water column, especially in waters with low K_d . Seasonal variability of
191 photochemical quenching has been observed, particularly during the spring to summer transition when
192 solar radiation is increasing, with the intensity of fluorescence quenching reduced at greater depth.
193 Correction of CHL concentrations where needed were computed from fluorescence that exhibited the
194 daily quenching near the surface (Sackmann et al., 2008; Xing et al., 2012), using as a reference the
195 MLD.



196 Because there is a linear relationship between the apparent oxygen utilization (AOU) and nitrate
197 concentration we use AOU to estimate available nitrate in the water column (Naqvi et al., 1986). Recent
198 evaluations of the relationship between AOU and nitrate plus nitrite (NO_x) have validated the
199 relationship describe by Naqvi et al. (1986) (Churchill et al., 2014; Zarokanellos et al., 2017b). Because
200 the regression intercepts the oxygen axis between 180-185 μM, we have used the 180 μM oxygen
201 isopleth as an index of the nitracline depth to examine the nutrient availability in the euphotic layer.

202

203 **2.2 Meteorological data**

204 The upper circulation of the CRS is strongly affected by the monsoonal reversal as the wind
205 convergence occurring in this area during winter gradually changes to a more uniform pattern of
206 northwest winds during summer (Zarokanellos et al 2017a). Although northwest winds prevailed over
207 our study throughout the year (Papadopoulos et al., 2013), it is unclear how air temperature, the wind
208 stress, and relative humidity affect the MLD in the Red Sea. Observation data sets from the
209 meteorological station of Yanbu airport, which is located approximately 12 km east of the glider
210 transect end point, have been used to investigate the relationship between the atmospheric forcing and
211 MLD in the CRS (Fig. 1b). Meteorological data, particularly 6 hour wind speed, air temperature, and
212 relative humidity, were obtained from the website
213 (http://rp5.md/Weather_archive_in_Yanbu_%28airport%29). Wind stress was calculated from wind
214 speed using the method of Large and Pond (1981). Wind speed, air temperature, and humidity were
215 acquired at 10 m height, and daily mean values span the period from December 2, 2014, to March 2,
216 2015.

217

218 **2.3 Satellite data**

219 To place the glider observations into the larger context of the CRS, ocean color images were
220 examined for the glider deployment period. MODIS Level-3 data were obtained from the NASA Ocean
221 Color Web (<http://oceancolor.gsfc.nasa.gov/>).

222

223 **2.4 Statistical analysis**



224 Pearson linear correlation coefficient was computed for 4 different wind speed ranges between
225 air temperature and relative humidity versus the daily mean MLD (Table 2; Sokal and Rohlf, 1969). To
226 exam the relationship between the atmospheric forcing (air temperature, relative humidity and wind
227 speed) with the integrated CHL, CDOM, bbp_{532} , and POC in the MLD Pearson correlation has been
228 applied (Table 4). The transect line has been separated in three subdivisions (AB, ABC, and CD) as
229 indicated in Fig. 1b, where mean subdivisions values for CHL, bbp_{532} , CDOM, POC, and POC:CHL
230 were calculated and have been binned (0.03°) latitudinally and longitudinally, respectively, for the
231 mixed layer, as Table 5 indicated. In addition, mean values of CHL, bbp_{532} , CDOM, and POC were
232 calculated for the first optical depth (Raitsos et al., 2013) and for the upper 200 m.

233 Principal component analysis (PCA) was used to investigate the linear relationship between
234 variables. In order to standardize the data forwards the variables have different units and magnitudes,
235 the PCA was performed using the correlation matrix instead of the covariance matrix. The following
236 data were used in the PCA analysis: potential (Temp), salinity (Sal), density (Den), oxygen (Oxy),
237 CDOM, bbp_{532} , and CHL. The data were divided in four depths categories to explore the vertical
238 distribution and the interactions of the physical and biochemical processes in the CRS (Table 3). We
239 partitioned data into the following depth bins (surface-to maximum depth, surface-20, 20-100 and 100-
240 200). Principal component analysis is used to explain the correlations between the variables for each
241 depth bin.

242

243 3. Results

244 3.1 Atmospheric conditions in the central Red Sea during winter/early spring

245 Model analyses of the Red Sea indicate the importance of the wind forcing in the Red Sea
246 circulation (Clifford et al., 1997; Patzert, 1974; Quadfasel D, 1993; Sofianos and Johns, 2003; Yao et
247 al., 2014a, 2014b). The location of the convergence zone between northerlies and southerlies in the
248 central Red Sea plays a crucial role in the forcing of Red Sea circulation and waves during the winter
249 when winds in the southern half of the Red Sea are southerly (Langodan et al., 2015). The atmospheric
250 data allow us to understand the important role of wind speed during the winter mixing period and how
251 this affects the deep chlorophyll maximum (DCM). The air temperature, wind stress and relative



252 humidity from the meteorological station reveals the arrival of cold, intense northerly winds (Fig. 2).
253 The intense wind stress of more than 0.004 N m^{-2} is associated with low relative humidity and producing
254 mixing of the upper layer. The sea temperature follows the similar distribution with the air temperature.
255 However, a time lag has been observed between the response of air temperature and sea temperature
256 (5m; Fig. 2a). Air temperature fluctuations have been observed during the winter/early spring period,
257 with the daily mean air temperature reached the minimum at 11th of January ($15.2 \text{ }^\circ\text{C}$) and the daily
258 mean MLD the maximum depth (85m) as the Fig. 2a and 2d indicated. A correlation between wind
259 stress and MLD has been observed as indicated in the Fig. 2b and 2d. To determine the dependence of
260 the MLD on wind speed, air temperature and relative humidity the data were subdivided into four wind
261 categories in order to separate the effects of the wind from air temperature and relative humidity. We
262 categorize the wind into low wind speed ($0\text{-}2 \text{ m s}^{-1}$), medium wind speed ($2\text{-}4 \text{ m s}^{-1}$), higher wind speed
263 ($4\text{-}7 \text{ m s}^{-1}$) and the entire range ($0\text{-}7 \text{ m s}^{-1}$; Table 2). The correlation coefficient r is significant ($p < 0.05$)
264 between air temperature and MLD for the first and third wind speed category, but the linear relationship
265 is weak (~ 0.3). Furthermore, the relative humidity and MLD correlation coefficient r is significant
266 ($p < 0.05$) for first, three and last wind speed category (Table 2). Although, strong (negative) linear
267 relationship (< -0.7) has been observed only in the last category.

268

269 **3.2 Physical and chemical variability.**

270 Based on the physical processes that occurred in the study area during the winter/early spring
271 period, three distinct periods; a) the first period is dominated by winter mixing, b) the second period is
272 characterized by intensification of the eddy circulation, and c) the last period demonstrate the
273 interaction between the EBC and the eddies. Winter mixing was observed between 2 December 2014 to
274 10 January 2015. The rapid increase of the MLD coincided with strong wind stress events in the CRS
275 (Fig. 2b and 2d). The eddy intensification spanned the period from 11 January until 10 February 2015,
276 when a CE and AE formed in the study area. During the existence of the eddy intensification, the
277 relative humidity and air temperature gradually increased, and the MLD became progressively
278 shallower. The EBC/ eddy interaction was discernible from 11 February until 2 March 2015. During this



279 time, the MLD progressively increased and two wind events accompanied by decrease air temperature
280 occurred.

281 Glider measurements show how the salinity, potential temperature, stratification (Brunt–Väisälä
282 Frequency; BVF), oxygen, and NO_x structure in the upper 400 m evolved during the winter/early spring
283 period (Fig. 3). The in situ observations illustrate the importance of winter mixing, the
284 physical/chemical role of the eddies, and EBC/eddies interaction. During the winter-mixing phase, the
285 MLD was highly variable extending from 8 to 88.2 m (mean 34.8 m, STD=24.5 m). During both
286 deployments, the euphotic zone range from 83.5 m to 126.2 m (mean 104.4 m, STD=7 m).

287 The glider observations reveal that the mixing events homogenized the upper layer to as deep as
288 90 m and as a result stratification is weak ($N^2 \sim 0$) as shown in Fig. 3a-b, and 3h. This weak stratification
289 extended to the depth of the permanent pycnocline, located between the 26 and 27.5 kg m⁻³ σ_θ (Fig. 3c).
290 The intense winter mixing thus oxygenates the upper layer to the depth of the mixed layer. During this
291 period, a small cyclonic eddy (CE) developed at the end of December 2014. The effect of the eddy was
292 to elevate the pycnocline reducing the MLD and lifting lower oxygen water into the upper layer (Fig.
293 3d). As with other variables the elevation of pycnocline brought nutrient containing water nearer to the
294 surface (Fig. 3e).

295 After the winter mixing period, the CE and AE eddies appears to intensify in the study area (Fig.
296 3f and 3g). Temperature decreased ($\Delta\theta \sim -2$ °C) and salinity ($\Delta S \sim 0.3$) increased rapidly in the upper
297 100m in a period of about 10 days (not shown here). The undulations of the pycnocline and isopleths of
298 other variables reflect the influence of the eddies on the hydrography of the region (Fig. 3f-j). In the
299 upper 100 m, the core of the CE is saltier (>40.2) and cooler (23.5 °C) than the surrounding water. In
300 contrast, the AE entrains warmer (> 25 °C) and less salty (39.8) water in its upper core. During the eddy
301 intensification period, the main pycnocline has significant weakens as indicated by the BVF (Fig. 3h).
302 Our observations show the development of the seasonal pycnocline at the end of January. The seasonal
303 pycnocline as indicated by the BVF follows the $\sigma_\theta = 27$ kg m⁻³ isopycnal. The high BVF associated
304 with $\sigma_\theta = 28$ kg m⁻³ isopycnal suggest that this density surface is good indicator of the permanent
305 pycnocline. Eddies during this period have an important role in modulate the vertical oxygen
306 distribution in the CRS (Fig. 3i). The highest oxygen concentrations (>200 μ M) are observed at the core



307 of AE where the maximum concentrations penetrate to 90m. The thickness of the high oxygen layer
308 ($>200 \mu\text{M}$) decreased from 90m in the center of AE to less than 60m in the core of the CE. Based on
309 Naqvi et al. (1986) and Churchill et al., (2014) measurable NO_x begins to appear at an AOU of about
310 $10\text{--}11 \mu\text{M}$. Thus, the top of nitricline lines up approximately with the $\sigma_\theta = 28 \text{ kg m}^{-3}$ isopycnal within
311 the eddies we see an elevation of this isopycnal from more 190m to less than 125m (Fig. 3i and 3j).
312 Within the AE, high oxygen concentrations ($>180 \mu\text{M}$) extend as deep as 200 m.

313 During EBC/eddies interaction period, lower salinity, warm water was found in the upper 100m
314 in the southern part and extended until 23.1°N (Fig. 3k and 3l). The fresher, warmer water is consistent
315 with entrainment of water from the northward transport of Gulf of Aden water via the EBC as
316 previously described by Zarokanellos et al., (2017a and 2017b). During this period, the AE occupies the
317 south part of the study area. The AE entrains the EBC water of the center of AE and likely redirects the
318 EBC offshore around the periphery of AE (Fig. 3l). Zarokanellos et al. (2017b) observed similar
319 patterns in an earlier study in spring 2013. During EBC/eddies interaction period, the stratification
320 (BVF) increased in the upper 100 m (Fig. 3m). The presence of the EBC contributed to the increase of
321 stratification, as it advected warmer, fresher water into the region. Within the CE, the $\sigma_\theta = 28 \text{ kg m}^{-3}$
322 isopycnal rises from 220 m to 160 m in the core of the eddy. The CE lifts low oxygen, nutrient-rich
323 water toward the upper layer (Fig. 3n and 3o). An overall reduction of oxygen ($<205 \mu\text{M}$) occurred in the
324 late winter/early spring (Fig. 3n). Very likely this reduction is associated with rising temperature
325 decreasing the oxygen saturation concentration. High values of the oxygen concentration ($>205 \mu\text{M}$) in
326 the surface layer were present in the core of the CE for the upper 60 m.

327

328 **3.3 Bio-optical variability.**

329 In the CRS generally, ocean color CHL is often a useful tracer to detect mesoscale eddies and to
330 understand of the biogeochemical processes associated with these features. Significant variations of
331 CHL, bbp_{532} , CHL to bbp_{532} ratio, CDOM, and POC were observed along the glider track during the
332 winter/early spring period (Fig 4). Winter mixing and mesoscale eddy activity enhanced CHL
333 concentration in the ML during this period. Mean CHL concentration in the ML (0.118 ± 0.017) during
334 the observation period was higher than the integrated CHL (0.0984 ± 0.015 ; 0-200m). During the



335 mixing period, deep mixing distributed the phytoplankton through the mixed layer, increasing the signal
336 detected by ocean colour imagery but without a corresponding increase in integrated chlorophyll (0-200
337 m; Fig 4a). This temporal increase of chlorophyll concentration during the mixing period results from
338 entrainment of the deep chlorophyll maximum (DCM) into the mixed layer. These unstable conditions
339 of the upper layer (especially during the intense wind events) may obscure the biologically driven diel
340 cycle in the region. During the mixed period, relatively high concentrations of bbp_{532} ($\sim 10^{-3}$) have been
341 observed in the mixed layer and associated in several cases with high CHL concentration (Fig 4b). High
342 CHL: bbp_{532} ratios have been observed primarily in the DCM and locally in the core of the CE where
343 CHL is elevated (Fig 4c). Moreover, a high CHL: bbp_{532} ratio occurred after wind stress events with a
344 time lag of a few days. The wind stress events cause deepening of the mixed layer and increase
345 temporarily the available nutrients. During the mixed period, low (< 0.5 ppb) CDOM concentration has
346 been identified in the MLD (Fig 4d). CDOM generally increases with depth, with the maximum
347 concentration appearing below 300 m. CHL concentration covary with POC as shown in Fig 4a and 4e.
348 Within the center of the CE eddy, the bulk of POC was located of the upper 60 m, where its
349 concentration was greater than 16 mg C m^{-3} .

350 Throughout the intensification of the eddy circulation period, rapid changes in the density are
351 related with the eddy structure in the region. Deepening of the mixed layer increases nutrient
352 availability resulting in increased CHL concentration. The highest CHL concentration occurred in the
353 center of the mesoscale CE eddy where the MLD shoaled from ~ 100 to 20 m (Fig. 4f). Subduction
354 occurred at the interface of the CE and AE eddy, resulting in higher CHL ($> 0.4 \text{ mg m}^{-3}$) and bbp_{532}
355 ($> 1.2 \times 10^{-3} \text{ m}^{-1}$) abundance at the boundary (Fig. 4f-g). High CHL: bbp_{532} ratios have been observed in
356 the DCM at the interface of the CE and AE as indicated at Fig. 4h. Variation in CDOM distribution was
357 observed in the upper 200 m where the eddy pair occurred (Fig. 4i). Low concentration of CDOM (< 0.5
358 ppb) was present primarily in the upper layer where σ_{θ} was less than 27.5 kg m^{-3} . CDOM concentration
359 was elevated (depressed) in the center of the CE (AE). The overall POC concentration increased during
360 the intensification of the eddy period for the upper 100 m, and subduction of POC occurred at the
361 interface between the AE and CE (Fig. 4j). During this period, the highest POC concentration was
362 observed at the core of the CE reaching up to 24 mg C m^{-3} .



363 During the EBC/eddy interaction period, water with a high concentration of CHL ($>0.4 \text{ mg m}^{-3}$)
364 was observed between 50 to 90 m, where the density anomaly was approximately 26 kg m^{-3} (Fig. 4k).
365 Figure 4l shows that higher bbp_{532} ($>10^{-3} \text{ m}^{-1}$) is associated with warmer and fresher water in the upper
366 70 m. bbp_{532} was greater than $1.2 \times 10^{-3} \text{ m}^{-1}$ in the core of the CE. The CHL: bbp_{532} ratio could be higher
367 in the DCM layer and at intermediate depths coinciding with the 26 kg m^{-3} isopycnal (Fig 4m).
368 Zarokanellos et al. (2017b) used low salinity and elevated CDOM at intermediate depths to distinguish
369 Gulf of Aden Intermediate Water (GAIW) in the CRS. The water along the 26 kg m^{-3} isopycnal where
370 both CHL and CDOM are elevated relative to the surrounding water is consistent with the GAIW
371 described by Zarokanellos et al. (2017b). GAIW was detectable from the southern end of the transect
372 until $\sim 23^\circ \text{N}$, where the EBC and the CE intersected. Low concentration of CDOM ($<0.5 \text{ ppb}$) is present
373 at intermediate depths in the center of the CE (Fig. 4n). Higher concentrations of POC ($>30 \text{ mg C m}^{-3}$)
374 and CHL (0.4 mg m^{-3}) were detected in the core of the CE (Fig 4o). Through the EBC/eddy interaction
375 period, CHL and POC covaried (Fig. 4k and 4o). Subduction of CHL, bbp_{532} , and hence POC is
376 indicated by the downward projection along the 27.5 kg m^{-3} isopycnal southward from the eddy center
377 (Fig. 4k, 4i and 4o).

378

379 **3.4 Water masses characteristics.**

380 Water masses characteristics underwent significant transition during the winter/spring period.
381 The potential temperature-salinity (Θ/S) diagram from both glider missions is shown in Fig. 5, where
382 the separate panels are color-coded for time, CHL, CDOM, and oxygen concentration. The most
383 distinctive feature of the Θ/S distribution is the very abrupt transition from relative diffuse Θ/S
384 distribution in the upper layer prior mid-January to a tight, linear Θ/S pattern in the upper layer after
385 mid-January. This abrupt transition appears to be due to the intensification of the CE lifting the 27.5 kg
386 m^{-3} isopycnal to near the surface and the arrival of low salinity water presumably from the Gulf of
387 Aden. The association with salinity range 39-39.4 psu, higher CHL ($>0.3 \text{ mg m}^{-3}$) and CDOM (>0.9
388 ppb) for density anomalies between 26 and 26.5 kg m^{-3} (Fig. 5b and 5c) is consistent with the
389 descriptions of GAIW provided by Churchill et al. (2014) and Zarokanellos et al. (2017b). GASW is
390 distinguished from GAIW, as it is warmer ($>26^\circ \text{C}$), less saline ($<39 \text{ psu}$), lower in CDOM ($<0.9 \text{ ppb}$)



391 and less dense ($\sigma_{\theta} < 26 \text{ kg m}^{-3}$). In this set of observations, oxygen does not show a significant
392 difference between GASW and GAIW (Fig. 5d). Oxygen in the upper layer ranged from 170 to 200
393 (μM) between the 25.3 and 27.5 $\text{kg m}^{-3} \sigma_{\theta}$. The maximum oxygen concentrations (210 to 220 μM) in
394 the surface water have been associated with the two strong wind events in the middle of December 2014
395 (Fig. 2b) that induced strong mixing that ventilated the surface layer. Above densities of 28 kg m^{-3} ,
396 oxygen concentration decreases from 150 to 20 (μM) at the depth of the oxygen minimum.

397

398 **3.5 Physical and biological variability in time and space.**

399 The CRS has been characterized as having high mesoscale activity and is one of the most
400 oligotrophic areas of the Red Sea (Raitsos et al., 2013; Zhan et al., 2014). Until recently, the physical
401 and biological variability have been examined with models, remote sensing studies, and infrequent in
402 situ observations. This data set provides the first glimpse of the significant changes that can occur in a
403 relatively short time period during the winter/early spring. Vertical profiles of the mean and standard
404 deviation (STD) of salinity, pot. temperature, CHL, CDOM, bbp_{532} , and POC illustrate the magnitude of
405 the variability that was observed in this period (Fig. 6). The data was parsed into three time-periods
406 based the vertical structure and spatial heterogeneity of the water masses in the upper layer. The bulk of
407 the variability, particularly in optical variables, occurred in the upper 200m (Fig. 6). This is consistent
408 with previous observations of eddy structure in CRS where evidence of the eddy penetrated to at least
409 200m (Zarokanellos et al., 2017a). Throughout the winter mixing period, the upper layer is
410 homogenized of reducing the variability of the upper layer. During the eddy intensification period, we
411 observed the greatest variability. This variability was likely due to seasonal transition and significant
412 horizontal exchange through the interaction of complex eddy activity. The upper layer variability was
413 again reduce when the EBC brought Gulf of Aden water that constrain the variability of the upper layer.

414 While remote sensing of ocean color data has provided significant insight into the temporal and
415 spatial variability within the first optical depth (nominally $\sim 20 \text{ m}$) of the Red Sea, the patterns might
416 not necessarily represent the variability of the upper 200m. This is most evident in the comparison of
417 the upper 20 m CHL versus the integrated CHL of 200 m (Fig. 7). In this case, the upper layer shows an
418 increase in the near surface CHL of more than 50 %. Figure 7 shows box-and-whiskers plots providing



419 the mean values and standard deviations of the variables CHL, bbp_{532} and CDOM for latitudinal (6
420 transects; 2 AB and 4 ABC) and longitudinal (4 transects CD) sections of both glider deployments. The
421 increase of the CHL in the first 20m results from deep mixing which entrains the DCM into the mixed
422 layer but without a net increase of the integrated water column CHL. This mixing is clearly evident in
423 the CHL distribution and MLD shown in Fig 4a. During the eddy intensification period CHL
424 concentration in the upper 20 m decrease as the DCM reformed but without significant change in the
425 integrated water column CHL (Fig 4a and Fig 7). However, along the line CD surface bbp_{532} , integrated
426 CDOM and integrated bbp_{532} increased during the eddy intensification phase. These increases are likely
427 due to enhanced along coast transport. During the EBC/eddy interaction period, both surface and
428 integrated bbp_{532} increased along with integrated CHL. Despite the increase of integrated CHL the
429 surface CHL continuous to decrease (Fig. 7a-b). These results indicate that there is not always a tight
430 relationship between bbp_{532} and CHL.

431

432 **3.6 Environmental factors controlling the optical properties.**

433 As described above, significant physical and optical variability occurred during the winter/early
434 spring period. To further characterize this variability principal component (henceforth PC) analysis was
435 used to determine the main modes of variability within the data. For the PC analysis, the data were
436 subdivided into four depth regions a) the upper 200m, b) surface layer to the first optical depth, c) DCM
437 region (20-100 m), and d) sub-euphotic region (100-200 m). Our aim is to reduce the effects of the
438 vertical variability of the physical and biological factors. The first two PCs accounted for 90.3% of the
439 variance for the upper 200m, 59% for the surface layer, 64.4% for the DCM layer, and 81% for the sub-
440 euphotic layer. Table 3 indicates the loading for the first two PCs and the relationships with respect of
441 each variable. For the upper 200m, PC1 explains 81.8 % of the total variance and was characterized by
442 negative loading in potential temperature, oxygen, CHL, and bbp_{532} , and positive in salinity, density,
443 and CDOM (Table 3). The first PC generally accounts for the vertical structure of water column. For the
444 second PC, CHL, CDOM and oxygen show similar absolute magnitude but oxygen was in opposite in
445 sign to CHL and CDOM. Within the upper 100 m salinity along with oxygen concentration are opposite



446 in sign to CHL and CDOM. This pattern of loadings is consistent with the characteristics of GAIW
447 where lower salinity, lower oxygen GAIW is accompanied by higher CHL and CDOM concentrations.

448 For the surface layer (0-20m), the first component is dominated by the physical variables (T, S,
449 σ_t) where T is opposite in sign with S and σ_t . The second component characterizes the bio-optical
450 variability where CHL, CDOM and bbp_{532} are opposite in sign with oxygen. The first two components
451 that characterize the DCM follow a similar pattern with the upper 200m. PC1 was dominated by the
452 physical variables and oxygen concentration. Within PC1 temperature and oxygen are opposite in sign
453 with salinity and σ_t similar with PC1 of the overall structure of the water column. The bio-optical
454 variables were more significant in PC2. In the sub-euphotic region, the PC1 again dominated by the
455 physical parameters. PC2 is dominated primarily by bbp_{532} .

456

457 **4. Discussion.**

458 Red Sea is a marginal sea affected by strong evaporation. When evaporation is accompanied by
459 significant cooling the water column stratification weakens such as strong surface forcing can cause
460 deep vertical mixing. If the mixing penetrates the nutricline, water column productivity may increase
461 due to the injection of nutrients in the euphotic zone. To investigate the effect of atmospheric forcing on
462 the biological distributions of CHL, CDOM, bbp_{532} , and POC of the ML, correlation coefficients were
463 calculated between characteristic atmospheric variables (air temperature, relative humidity, and wind
464 speed) and biological variables (CHL, CDOM, bbp_{532} , and POC) in the ML for both glider missions
465 (Table 4). The negative relationship of air temperature and relative humidity with CHL (-0.46 & -0.47)
466 and CDOM (-0.47 & -0.34) is consistent with weakened stratification resulting from cooler temperature
467 and increase salinity. The weakened stratification allows for mixing that penetrates the pycnocline
468 entraining deeper water that contains higher CDOM and nutrients concentrations. CHL and CDOM are
469 weakly correlated with the wind speed (0.32 & 0.30, respectively). No significant correlations exist
470 between wind speed with bbp_{532} and POC.

471 Mean values of CHL, CDOM, bbp_{532} , POC, and POC:CHL in the mixed layer were calculated
472 separately for the two legs of the glider pattern (Table 5). The mean CHL concentration in the mixed
473 layer is 0.12 mg m^{-3} . CHL concentrations along segments ABC-1 to ABC-3 increased by nearly 50%



474 when deep mixing and mesoscale eddy activity were present. CHL increased along the segment CD-2
475 when an intrusion of GAIW occurred (Fig. 3b). Increase of CDOM concentration in the mixed layer has
476 been observed under two processes during the winter. Mesoscale eddies are one process that results
477 vertical transport of sub-pycnocline water that would contribute to increase CDOM in the upper layer.

478 Lateral advection of GAIW containing elevated CDOM can also contribute CDOM to region
479 (GAIW; Zarokanellos et al 2017b). An overall latitudinal increase of CDOM has been revealed between
480 transects ABC-2 to ABC-4 (Fig. 7f). Moreover, enhanced of CDOM has been also observed in the
481 longitudinal transects between the CD-2 and CD-4. The overall bbp_{532} concentration in MLD during the
482 study period was $8.77E-04$. GASW appears in CRS in the late winter/early spring and is correlated with
483 elevated bbp_{532} , under the assumption that phytoplankton CHL decomposes faster than total organic C.
484 POC:CHL ratio has been used to differentiate when or where autotrophic processes dominate
485 (POC:CHL<200) versus heterotrophic processes (POC:CHL>200; Bentaleb, 1998; Cifuentes et al.,
486 1988). Heterotrophic remineralization by microbial organisms is understood to dominated when the
487 POC:CHL ratio is greater than 200-300 (Bentaleb, 1998; Cifuentes et al., 1988). Based on these
488 assumptions, heterotrophic remineralization was important at the beginning of the winter period as
489 shown on Table 5. After the first mixing event in December 2014, the contribution of autotrophic
490 processes in the mixed layer increases based on the decrease of the POC:CHL ratio (<160).

491 The mechanisms that generate and sustain mesoscale eddies in the CRS are so far poorly
492 understood. In the oligotrophic CRS, there is an inconsistency of nutrient supply and replacement in the
493 euphotic zone. Vertical exchange between the sub-pycnocline region and the euphotic zone is essential
494 for phytoplankton growth and productivity. Mesoscale eddies in the CRS have a large biogeochemical
495 affect not only in the CRS but contribute to the larger-scale processes in the northern half of the Red
496 Sea (Zarokanellos et al 2017a, b). Globally, oligotrophic waters can contribute more than 30% of the
497 marine carbon fixation and efficiently transfer atmospheric CO_2 to the ocean interior via physical and
498 biological pumps (Marañón et al., 2003; Moutin and Prieur, 2012). The export of organic carbon from
499 the surface product layer to the deeper ocean is a critical component of the carbon cycle. Many studies
500 until now, provide controversial results about the POC flux between cyclonic and anticyclonic eddies
501 (see Table 1; Shih et al., 2015).



502 During the eddy intensification period, eddies have a key role in the exchange of water mass
503 characteristics and optical properties between the northern and the southern regions of the Red Sea
504 (Zarokanellos et al., 2017a). Glider observations and satellite chlorophyll have been used to characterize
505 not only the horizontal but also the vertical distributions of CHL. Figure 8 shows coincident in-situ and
506 remote sensing observations of CHL, bbp_{532} and CDOM during 1 to 11 February, 2015. The in-situ
507 observations reveal subduction of CHL and suspending particles (bbp_{532}) at the interface of the eddy
508 pair and elevated concentration of CHL, and bbp_{532} has been observed at the edge of the AE (Fig 8 and,
509 9b). Maximum integrated CHL concentrations occur at the interface between AE and CE features where
510 the subductive CHL of the CE and the shallower DCM of the AE overlap (22.9 °N; Fig. 8d). In the same
511 period, the EBC that brings low salinity and rich in nutrients water (GAIW) at intermediate depths in
512 the CRS. GAIW has been characterized by elevated CHL and CDOM concentrations and lower salinity
513 (Fig 8a, 8c and 3i). The arrival of the EBC advects both GAIW and GASW into the region where both
514 water masses contain high bbp_{532} (Fig. 8b and 8c). The AE accumulate GASW and GAIW in the core of
515 the eddy and as result elevate normalize average and integrated CHL has been observed (Fig 9d). The
516 CE enhances the upward displacement of deep, nutrient rich water to the euphotic zone. The latter
517 contribute in the increase of CHL, bbp_{532} and CDOM at the core of the CE, which located at ~23.3 °N.

518 Remote sensing analyses indicate that the eddy activity contributes to horizontal CHL
519 dispersion including the exchange between open sea and coastal environments. An ongoing question
520 has been whether the surface ocean color signal associated with eddies are truly chlorophyll signatures
521 or perhaps CDOM or particulate organic material that originates from coastal regions. Based on the
522 comparison of the in-situ glider observations with the remotely sensed ocean color in this example it
523 appears that the signature is generally chlorophyll that results from the interaction of the eddy with the
524 ambient ocean. Eddies spanning the basin width can interact with the coastal region entraining organic
525 matter from shallow coastal environments and transport that across the width of the basin (Fig. 8e and
526 8f). The biogeochemical response to the subsurface physical processes provides a sensitive indicator to
527 the processes that result from the mixing and eddy dynamics – processes that are not necessarily
528 detectable via remote sensing.



529 In general, the export of POC, estimated from bbp532, from the euphotic zone of the ocean is
530 primarily considered to be due to sinking of phytoplankton, particulate aggregates, and fecal material
531 (Durkin et al., 2016; Siegel et al., 2014). In this study, we show that the interface of the eddy pair
532 subduction of particles from the surface layer ($\geq 100\text{m}$) transports them to depths of nearly 200m
533 beneath the interface. This results is consistence with the growing body of literature that demonstrates
534 the importance of eddies and fronts in the downward flux of organic matter beneath the euphotic zone
535 (Ashjian et al., 2006; Jones, 1991; Kadko et al., 1991; Shih et al., 2015; Stukel et al., 2017; Washburn et
536 al., 1991)

537 A fundamental question of understanding Red Sea is how Gulf of Aden Water interacts with the
538 Red Sea. It is generally understood that GASW enters the Red Sea during September to May under the
539 influence of the north-east monsoon (Murray and Johns, 1997; Smeed, 2004; Sofianos et al., 2002; Yao
540 et al., 2014a) and GAIW enters during the period of the south-west monsoon when winds in the
541 southern Red Sea are toward the south-southeast. GAIW is known to be low in oxygen, high inorganic
542 nutrients and elevated in CHL (Churchill et al., 2014; Sofianos and Johns, 2007; Wafar et al., 2016;
543 Zarokanellos et al., 2017a). Recent results show that GAIW also contains elevated CDOM fluorescence
544 (Zarokanellos et al., 2017b). The advection of low salinity water into the study region appears from the
545 TS perspective to be GASW that has enter during the winter period. However, embedded within the TS
546 structure is a subsurface region where both CDOM and CHL concentration are elevated above the water
547 with lower and higher densities along where appears to be a simple mixing line. A possible explanation
548 of this could be there under strong wind forcing near the strait of Bab en Mandab flow of Gulf of Aden
549 Water into the Red Sea may entrain some GAIW as well as GASW. Thus the winter injections of water
550 of the Gulf of Aden may also enhance the nutrient flux and productivity of the Red Sea but not to the
551 extent of the summer GAIW intrusions.

552 Vertical chlorophyll distributions can provide an indication of nutrient availability, and the role
553 of intrusion from Gulf of Aden Intermediate Water (GAIW) in the CRS. GAIW is characterized by low
554 salinity, high CDOM and nutrient concentration (Zarokanellos et al., 2017b). GAIW is the primary
555 source of nutrients into the Red Sea (Naqvi et al., 1986; Souvermezoglou et al., 1989). However, its
556 spatial distribution and its contribution to primary production within the basin remains unclear. Previous



557 studies have shown that GAIW intrusions are seasonal and episodic in character (Churchill et al., 2014;
558 Sofianos and Johns, 2007; Zarokanellos et al., 2017b). GAIW intrusions affect both physical and
559 biogeochemical properties of the water. Once it has entered the Red Sea, northward advection of GAIW
560 modifies its physical and optical characteristics as the result of solar insolation, strong evaporation and
561 mixing with ambient Red Sea water (Fig 3k-l, 3n, 4k, and 4n). Nutrients become diluted and depleted as
562 the GAIW advects northward. High CHL concentrations in the DCM are not always dependent on the
563 presence of GAIW, but also depend on eddy activity that can elevate subpycnocline nutrients into the
564 photic layer. GAIW, typically located between the 26 and 26.5 kg m⁻³ isopycnals has been characterized
565 by high concentration of CDOM (>0.9 ppb) and CHL (>0.4 mg m⁻³; (Zarokanellos et al., 2017b).
566 During the EBC/eddy interactions both GASW and GAIW were detected in the study area below 23 °N.
567 These two water masses differ not only in their thermohaline characteristics, but also show distinct
568 optical signatures.

569 Figure 9a shows a positive relationship between CHL and bbp_{532} where the data are color coded
570 according to salinity. For salinities less than 39.4 psu and densities of 26 kg m⁻³ or greater, GAIW can
571 be distinguished from GASW, by CHL concentrations >0.4 mg m⁻³.and CDOM concentration >0.9 ppb
572 (not shown here; Zarokanellos et al., 2017b). Figure 9b illustrates the same relationship but color-coded
573 into 3 depth categories: a) surface layer to 20 m (approximately the first optical depth); b) 20 m-100 m,
574 incorporating the DCM region; and c) the upper 200m. High values of bbp_{532} occurred in the first depth
575 category (0-20m), during winter and early spring period. CHL concentrations were low in this layer.
576 Because we do not see significant diel variability in the CHL layer we conclude that this CHL
577 fluorescence is not due to quenching. The high bbp_{532} , low CHL water is associated low salinities that
578 was conclude that the water is GASW but we cannot characterize the nature of the particles in this
579 dataset. In the DCM layer, CHL and bbp_{532} are highly correlated. Vertical elevation of the nutricline,
580 subduction of organic matter and lateral advection are some of the physical processes that affect the
581 optical characteristics of GASW and GAIW during their northward transport along the eastern boundary
582 of the Red Sea.

583

584 **5. Summary and conclusions**



585 The Red Sea's significant latitudinal range from 10°N to 30°N creates a thermohaline circulation
586 that has similarities to larger scale ocean basins such as the Atlantic Ocean. In addition to its large-scale
587 circulation, mesoscale circulation patterns are ubiquitous within the basin. The basin responds to
588 various large-scale climatological forcing processes such as ENSO and North Atlantic Oscillation.
589 Warming of the upper layer increases stratification, thus reducing vertical mixing and the flux of
590 nutrients into the upper layer. Consequently, this stratification limits primary production. Because of
591 these characteristics, the Red Sea provides a laboratory for understanding the influence of climate
592 change on the physics and biogeochemistry of the upper ocean. Despite its potential importance for
593 understanding this until recently, limited knowledge has been available regarding dynamics of the Red
594 Sea.

595 In-situ and remote sensing observations have been used in this study to investigate the response
596 of physical and biological processes to atmospheric forcing during the winter and early spring period.
597 Our findings provide new observations of the physical and biological responses in the CRS. The glider
598 observations reveal temporal and spatial responses to atmospheric forcing. The responses include
599 vertical mixing, mesoscale eddies and lateral advection that are otherwise difficult to resolve with more
600 traditional ship-based or moored observations. Within this study both anticyclonic and cyclonic were
601 apparent during the observational period.

602 During the winter period, surface cooling and strong winds caused mixing in the upper 100m.
603 The intense mixing affects the distribution of all properties, including bio-optical properties. The deep
604 mixing redistributed the phytoplankton from the DCM through the mixed layer increasing the
605 concentration in the upper water column thereby increasing the chlorophyll detected by MODIS.
606 Despite the increase in nearsurface chlorophyll, the integrated (0-200m) CHL remained essentially
607 constant. The strong mixing events created the pre-conditions for the development of a mesoscale CE at
608 the end of December 2015 (Fig 3a and 3b). The mesoscale CE elevated nutrient-bearing subsurface
609 water into the euphotic zone leading to an increase in CHL concentration (Fig 4a). High concentration
610 of bbp_{532} and POC has were also observed in the center of mesoscale CE (Fig 4b and 4e). During the
611 eddy intensification period, weakening of stratification and shallowing of the MLD was observed (Fig
612 3h). The structure of the density field suggests both a CE and AE were present. Within the CE



613 integrated chlorophyll and estimated POC concentrations (0-200m) were higher where the isopycnals
614 were uplifted, suggesting a response to shallowing of the nutricline in central region of eddy (Fig. 4f
615 and 4j). In February, deepening of the DCM along with the isopycnals along the southern boundary of
616 the CE and the two chlorophyll maximum layers indicates subduction at the boundary between the two
617 features. At this interface where the two CHL layers occur, the integrated CHL and bbp_{532}
618 concentrations are higher than to either side of the interface. During EBC/eddy interaction period,
619 northward transport along the northeastern boundary of the eddy is consistent with the presence of the
620 EBC in the CRS. During this period, water that is identifiable with GASW and GAIW change modify
621 both thermohaline and optical characteristics. Throughout this period, glider observations show that the
622 main source of fresh and rich in nutrient water is present at intermediate depths where lateral advected
623 with the EBC. The interplay between the EBC and eddies, regulate the distribution of the GASW and
624 GAIW within the CRS.

625 Better understanding of the physical dynamics and ecological response of the region requires
626 continued long-term monitoring. In order to better understand the biogeochemical dynamics of the
627 region, further efforts require elucidation of the primary productivity response to seasonal, mesoscale
628 and longer term processes Autonomous underwater vehicles (AUVs) equipped with the appropriate
629 sensor suite enable monitoring of physical and biogeochemical properties over a range of temporal and
630 spatial scales, helping to achieve these goals. The direct and indirect effects of isopycnal displacement
631 on phytoplankton distribution and productivity, close alignment of physical and biological properties at
632 frontal boundaries, and variation of physical and biogeochemical features of eddies, underscore the
633 importance of high-resolution in situ measurements at appropriate scales. It is well known that eddies
634 and fronts contribute nutrients into the upper layer enhancing primary production, phytoplankton
635 biomass and particle concentration (Li et al., 2012; Ohman et al., 2012; Stramma et al., 2013). We
636 believe that continuing to study these processes in the globally extreme Red Sea will help us to better
637 understand the potential response of the global ocean to the current trends in climate.

638

639 Acknowledgements



640 The authors gratefully acknowledge the NASA Goddard Space Flight Center, Ocean Ecology
641 Laboratory, Ocean Biology Processing Group for remote sensing data used in this study. Datasets from
642 ocean color are freely accessible online on the official website (<https://oceancolor.gsfc.nasa.gov/>)
643 accessed on 18/09/2016. Glider data obtained from both glider missions can be obtained from Nikolaos
644 D Zarokanellos (KAUST) and Burton H. Jones (KAUST). The authors are grateful the KAUST Coastal
645 Marine Operation Lab (CMOR) for their engineering support during the glider deployments. Particular
646 thanks go to Sebastian Steinke, Brian Hession, Samer Mahmoud and Lloyd Smith for their help with the
647 glider deployments. Funding from King Abdullah University of Science and Technology (KAUST)
648 supported the research in this publication.

649

650 References

651 Acker, J., Leptoukh, G., Shen, S., Zhu, T. and Kempler, S.: Remotely-sensed chlorophyll a observations
652 of the northern Red Sea indicate seasonal variability and influence of coastal reefs, *J. Mar. Syst.*, 69(3–
653 4), 191–204, doi:10.1016/j.jmarsys.2005.12.006, 2008.

654 Ashjian, C., Arnone, R., Davis, C., Jones, B., Kahru, M., Lee, C. and Mitchell, B. G.: Biological
655 Structure and Seasonality in the Japan/East Sea, *Oceanography*, 19(3), 122–133,
656 doi:10.5670/oceanog.2006.49, 2006.

657 Behrenfeld, M. J., Kolber, Z. S., Field, C. B., Behrenfeld, M. J., Randerson, J. T., Falkowski, P. G.,
658 deBaar, H. J. W., Martin, J. H., Coale, K. H., Kolber, Z., Falkowski, P. G., Falkowski, P. G., Kolber, Z.,
659 Kolber, Z., Prasil, O., Falkowski, P. G., Murphy, L. S., Haugen, E. M., Gieskes, W. W., Kraay, G. W.,
660 Olsen, R. J., Chisholm, S. W., Zettler, E. R., Altabet, M. A., Dusenberry, J. A., Velduis, M. J. W.,
661 Kraay, G. W., Partensky, F., Blachot, J., Lantoiné, F., Neveux, J., Marie, D., Krause, G. H., Weis, E.,
662 Duce, R. A., Tindale, N. W., Allen, J. F., Allen, J., Bennett, J., Steinback, K. E., Arntzen, C. J.,
663 Mullineaux, C. W., Tobin, M. J., Jones, G., Burger-Wiersma, T., Post, A. F., Salehian, O., Bruce, D.,
664 Aoki, M., Katoh, S., Mullineaux, C. W., Allen, J. F., Scherer, S., Helmar, A., Böger, P., Dubinsky, Z.,
665 Falkowski, P. G., Wyman, K., Dau, H., Guikema, J. A., Sherman, L. A., Sandmann, G., Vassiliev, I. R.,
666 Greene, R. M., Geider, R. J., Kolber, Z. and Falkowski, P. G.: Widespread iron limitation of
667 phytoplankton in the south pacific ocean, *Science*, 283(5403), 840–3,



- 668 doi:10.1126/science.283.5403.840, 1999.
- 669 Belkin, I. M.: Rapid warming of Large Marine Ecosystems, *Prog. Oceanogr.*, 81(1–4), 207–213,
670 doi:10.1016/j.pocean.2009.04.011, 2009.
- 671 Bentaleb, I.: Carbon isotopic fractionation by plankton in the Southern Indian Ocean : relationship
672 between $\delta^{13}\text{C}$ of particulate organic carbon and dissolved carbon dioxide, *J. Mar. Syst.*, 17, 39–58,
673 1998.
- 674 Boss, E. and Pegau, W. S.: Relationship of light scattering at an angle in the backward direction to the
675 backscattering coefficient, *Appl. Opt.*, 40(30), 5503, doi:10.1364/AO.40.005503, 2001a.
- 676 Boss, E. and Pegau, W. S.: Relationship of light scattering at an angle in the backward direction to the
677 backscattering coefficient, *Appl. Opt.*, 40(30), 5503–5507, 2001b.
- 678 Boss, E., Picheral, M., Leeuw, T., Chase, A., Karsenti, E., Gorsky, G., Taylor, L., Slade, W., Ras, J. and
679 Claustre, H.: The characteristics of particulate absorption, scattering and attenuation coefficients in the
680 surface ocean; Contribution of the Tara Oceans expedition, *Methods Oceanogr.*, 7, 52–62,
681 doi:10.1016/j.mio.2013.11.002, 2013.
- 682 Bower, A. S., Swift, S. A., Churchill, J. H., McCorkle, D. C., Abualnaja, Y., Limeburner, R. and Zhai,
683 P.: New observations of eddies and boundary currents in the Red Sea, vol. 15, p. 9875., 2013.
- 684 de Boyer Montégut, C.: Mixed layer depth over the global ocean: An examination of profile data and a
685 profile-based climatology, *J. Geophys. Res.*, 109(C12), C12003, doi:10.1029/2004JC002378, 2004.
- 686 Brewin, R. J. W., Raitsos, D. E., Dall’Olmo, G., Zarokanellos, N., Jackson, T., Racault, M. F., Boss, E.
687 S., Sathyendranath, S., Jones, B. H. and Hoteit, I.: Regional ocean-colour chlorophyll algorithms for the
688 Red Sea, *Remote Sens. Environ.*, 165, 64–85, doi:10.1016/j.rse.2015.04.024, 2015.
- 689 Cantin, N. E., Cohen, A. L., Karnauskas, K. B., Tarrant, A. M., McCorkle, D. C. and Cantin, Neal E.,
690 Cohen, Anne L., Karnauskas, Kristopher B., Tarrant, Ann M., McCorkle, D. C.: Ocean Warming Slows
691 Coral Growth in the Central Red Sea, *Science* (80-.), 326(2010), 322–325,
692 doi:10.1126/science.1190182, 2010.
- 693 Cetinić, I., Perry, M. J., Briggs, N. T., Kallin, E., D’Asaro, E. A. and Lee, C. M.: Particulate organic
694 carbon and inherent optical properties during 2008 North Atlantic Bloom Experiment, *J. Geophys. Res.*
695 *Ocean.*, 117(C6), n/a-n/a, doi:10.1029/2011JC007771, 2012.



- 696 Chen, C., Li, R., Pratt, L., Limeburner, R., Berdsey, R., Bower, A., Jiang, H., Abualnaja, Y., Xu, Q.,
697 Lin, H., Liu, X., Lan, J. and Kim, T.: Process modeling studies of physical mechanisms of the formation
698 of an anticyclonic eddy in the central Red Sea, *J. Geophys. Res. Ocean.*, 119(Figure 3), 1445–1464,
699 doi:10.1002/2013JC009351. Received, 2014.
- 700 Churchill, J. H., Bower, A. S., McCorkle, D. C. and Abualnaja, Y.: The transport of nutrient-rich Indian
701 Ocean water through the Red Sea and into coastal reef systems, *J. Mar. Res.*, 72(3), 165–181,
702 doi:10.1357/002224014814901994, 2014.
- 703 Cifuentes, L. a., Sharp, J. H. and Fogel, M. L.: Stable carbon and nitrogen isotope biogeochemistry in
704 the Delaware estuary, *Limnol. Oceanogr.*, 33(5), 1102–1115, doi:10.4319/lo.1988.33.5.1102, 1988.
- 705 Clifford, M., Horton, C., Schmitz, J. and Kantha, L. H.: An oceanographic nowcast/forecast system for
706 the Red Sea, *J. Geophys. Res. Ocean.*, 102(C11), 25101–25122, doi:10.1029/97JC01919, 1997.
- 707 Durkin, C. A., Van Mooy, B. A. S., Dyrman, S. T. and Buesseler, K. O.: Sinking phytoplankton
708 associated with carbon flux in the Atlantic Ocean, *Limnol. Oceanogr.*, 61(4), 1172–1187,
709 doi:10.1002/lno.10253, 2016.
- 710 EDWARDS, F. J.: CHAPTER 3 – Climate and Oceanography, in *Red Sea*, pp. 45–69., 1987.
- 711 Ganssen, G. and Kroon, D.: EVIDENCE FOR RED SEA SURFACE CIRCULATION FROM
712 OXYGEN ISOTOPES OF MODERN SURFACE WATERS AND PLANKTONIC FORAMINIFERAL
713 TESTS, *Paleoceanography*, 6(1), 73–82, 1991.
- 714 Green, R. E., Bower, A. S. and Lugo-Fernández, A.: First Autonomous Bio-Optical Profiling Float in
715 the Gulf of Mexico Reveals Dynamic Biogeochemistry in Deep Waters, edited by W.-C. Chin, *PLoS*
716 *One*, 9(7), e101658, doi:10.1371/journal.pone.0101658, 2014.
- 717 Jones, B. H.: The Coastal Transition Zone: Nutrient Distributions and Transformations Associated with
718 Cool Filaments off Northern California, [online] Available from:
719 <http://www.dtic.mil/docs/citations/ADA238426> (Accessed 14 October 2017), 1991.
- 720 Kadko, D. C., Washburn, L. and Jones, B.: of Subduction Within of the Northern California that these
721 features may be a significant factor Point Arena (Figure 1). It involved and aging : processes, *J.*
722 *Geophys. Res. - Ocean.*, 96(C8), 14,909-14,926, 1991.
- 723 Kheireddine, M., Ouhssain, M., Claustre, H., Uitz, J., Gentili, B. and Jones, B. H.: Assessing Pigment-



- 724 Based Phytoplankton Community Distributions in the Red Sea, *Front. Mar. Sci.*, 4(May), 1–18,
725 doi:10.3389/fmars.2017.00132, 2017.
- 726 Kinkade, C. S., Marra, J., Dickey, T. D., Langdon, C., Sigurdson, D. E. and Weller, R.: Diel bio-optical
727 variability observed from moored sensors in the Arabian Sea, *Deep. Res. II*, 46, 1813–1831, 1999.
- 728 Langodan, S., Cavaleri, L., Viswanadhapalli, Y. and Hoteit, I.: Wind-wave source functions in opposing
729 seas, *J. Geophys. Res. Ocean.*, 120(10), 6751–6768, doi:10.1002/2015JC010816, 2015.
- 730 Large, W. G. and Pond, S.: Open Ocean Momentum Flux Measurements in Moderate to Strong Winds,
731 *J. Phys. Oceanogr.*, 11(3), 324–336, doi:10.1175/1520-0485(1981)011<0324:OOMFMI>2.0.CO;2,
732 1981.
- 733 Lee, C. M., Jones, B. H., Brink, K. H. and Fischer, A. S.: The upper-ocean response to monsoonal
734 forcing in the Arabian Sea: Seasonal and spatial variability, *Deep. Res. Part II Top. Stud. Oceanogr.*,
735 47(7–8), 1177–1226, doi:10.1016/S0967-0645(99)00141-1, 2000.
- 736 Li, Q. P., Franks, P. J. S., Ohman, M. D. and Landry, M. R.: Enhanced nitrate fluxes and biological
737 processes at a frontal zone in the southern California current system, *J. Plankton Res.*, 34(9), 790–801,
738 doi:10.1093/plankt/fbs006, 2012.
- 739 Longhurst, A. R.: THE INDIAN OCEAN, in *Ecological Geography of the Sea*, pp. 275–325, Elsevier.,
740 2007a.
- 741 Longhurst, A. R.: THE PACIFIC OCEAN, in *Ecological Geography of the Sea*, pp. 327–441, Elsevier.,
742 2007b.
- 743 Mahadevan, A.: Ocean science: Eddy effects on biogeochemistry, *Nature*, 506(7487), 168–169,
744 doi:10.1038/nature13048, 2014.
- 745 Maillard, C. and Soliman, G.: Hydrography of the Red Sea and exchanges with the Indian Ocean in
746 summer, *Oceanol. Acta*, 9(3), 249–269 [online] Available from:
747 <http://archimer.ifremer.fr/doc/00110/22113/19751.pdf>, 1986.
- 748 Marañón, E., Behrenfeld, M. J., González, N., Mouriño, B. and Zubkov, M. V.: High variability of
749 primary production in oligotrophic waters of the Atlantic Ocean: Uncoupling from phytoplankton
750 biomass and size structure, *Mar. Ecol. Prog. Ser.*, 257, 1–11, doi:10.3354/meps257001, 2003.
- 751 Martin, A. P. and Richards, K. J.: Mechanisms for vertical nutrient transport within a North Atlantic



- 752 mesoscale eddy, *Deep Sea Res. Part II Top. Stud. Oceanogr.*, 48(4–5), 757–773, doi:10.1016/S0967-
753 0645(00)00096-5, 2001.
- 754 McGillicuddy, D. J., Robinson, a. R., Siegel, D. a., Jannasch, H. W., Johnson, R., Dickey, T. D.,
755 McNeil, J., Michaels, a. F., Knap, a. H. and Jr, D. J. M.: Influence of Mesoscale Eddies on New
756 Production in the Sargasso Sea, *Nature*, 394(1977), 263–266, doi:10.1038/28367, 1998.
- 757 McGillicuddy, D. J., Anderson, L. A., Doney, S. C. and Maltrud, M. E.: Eddy-driven sources and sinks
758 of nutrients in the upper ocean: Results from a 0.1° resolution model of the North Atlantic, *Global*
759 *Biogeochem. Cycles*, 17(2), n/a-n/a, doi:10.1029/2002GB001987, 2003.
- 760 Morcos, S. A.: Physical and Chemical Oceanography of the Red Sea, *Ocean. Mar. Biol. Annu. Rev.*, 8,
761 73–202, 1970.
- 762 Morel, A.: Optical properties of pure water and pure sea water, *Opt. Asp. Oceanogr.*, 1, 1–24 [online]
763 Available from: <https://marine.rutgers.edu/pubsclassics/private/morel1974-water.pdf> (Accessed 22 June
764 2016), 1974.
- 765 Morel, A. and Maritorena, S.: Bio-optical properties of oceanic waters: A reappraisal, *J. Geophys. Res.*
766 *Ocean.*, 106(C4), 7163–7180, doi:10.1029/2000JC000319, 2001.
- 767 Moutin, T. and Prieur, L.: Influence of anticyclonic eddies on the Biogeochemistry from the
768 Oligotrophic to the Ultraoligotrophic Mediterranean (BOUM cruise), *Biogeosciences*, 9(10), 3827–
769 3855, doi:10.5194/bg-9-3827-2012, 2012.
- 770 Murray, S. P. and Johns, W.: Direct observations of seasonal exchange through the Bab el Mandab
771 Strait, *Geophys. Res. Lett.*, 24(21), 2557–2560, doi:10.1029/97GL02741, 1997.
- 772 Naqvi, S. W. A., Hansen, H. P. and Kureishy, T. W.: Nutrient-uptake and regeneration ratios in the red-
773 sea with reference to the nutrient budgets, *Oceanol. acta*, 9(3), 271–275 [online] Available from:
774 <http://archimer.ifremer.fr/doc/00110/22114/19752.pdf>, 1986.
- 775 Ohman, M. D., Powell, J. R., Picheral, M. and Jensen, D. W.: Mesozooplankton and particulate matter
776 responses to a deep-water frontal system in the southern California Current System, *J. Plankton Res.*,
777 34(9), 815–827, doi:10.1093/plankt/fbs028, 2012.
- 778 Papadopoulos, V. P., Abualnaja, Y., Josey, S. A., Bower, A., Raitzos, D. E., Kontoyiannis, H. and
779 Hoteit, I.: Atmospheric Forcing of the Winter Air–Sea Heat Fluxes over the Northern Red Sea, *J. Clim.*,



- 780 26(5), 1685–1701, doi:10.1175/JCLI-D-12-00267.1, 2013.
- 781 Patzert, W. C.: Wind-induced reversal in Red Sea circulation, *Deep. Res. Oceanogr. Abstr.*, 21(2), 109–
782 121, doi:10.1016/0011-7471(74)90068-0, 1974.
- 783 Pearman, J. K., Ellis, J., Irigoien, X., Sarma, Y. V. B., Jones, B. H. and Carvalho, S.: Microbial
784 planktonic communities in the Red Sea: high levels of spatial and temporal variability shaped by
785 nutrient availability and turbulence, *Sci. Rep.*, 7(1), 6611, doi:10.1038/s41598-017-06928-z, 2017.
- 786 Phillips, O. M.: On turbulent convection currents and the circulation of the Red Sea, *Deep Sea Res.*
787 *Oceanogr. Abstr.*, 13(6), 1149–1160, doi:10.1016/0011-7471(66)90706-6, 1966.
- 788 Quadfasel D, B. H.: Gyre-scale circulation cells in the Red Sea, *Oceanol. Acta*, 1993.
- 789 Qurban, M. A., Balala, A. C., Kumar, S., Bhavya, P. S. and Wafar, M.: Primary production in the
790 northern Red Sea, *J. Mar. Syst.*, 132, 75–82, doi:10.1016/j.jmarsys.2014.01.006, 2014.
- 791 Racault, M. F., Raitsos, D. E., Berumen, M. L., Brewin, R. J. W., Platt, T., Sathyendranath, S. and
792 Hoteit, I.: Phytoplankton phenology indices in coral reef ecosystems: Application to ocean-color
793 observations in the Red Sea, *Remote Sens. Environ.*, 160, 222–234, doi:10.1016/j.rse.2015.01.019,
794 2015.
- 795 Raitsos, D. E., Pradhan, Y., Brewin, R. J. W., Stenchikov, G. and Hoteit, I.: Remote Sensing the
796 Phytoplankton Seasonal Succession of the Red Sea, edited by I. Álvarez, *PLoS One*, 8(6), e64909,
797 doi:10.1371/journal.pone.0064909, 2013.
- 798 S.Morcós, G. F. S.: Circulation and deep water formation in the Northern Red Sea in winter,
799 *L’oceanographic physique de la Mer Rouge*, CNEXO, Paris , 91-103. - Google Scholar with H-Index
800 Calculator, “Circulation Deep Water Form. North. Red Sea Winter.” *L’oceanographic Phys. La Mer*
801 *Rouge*, 91–103, 1974.
- 802 Sackmann, B. S., Perry, M. J. and Eriksen, C. C.: Fluorescence quenching from Seaglider Seaglider
803 observations of variability in daytime fluorescence quenching of chlorophyll-a in Northeastern Pacific
804 coastal waters Fluorescence quenching from Seaglider, *Biogeosciences Discuss*, 5, 2839–2865 [online]
805 Available from: www.biogeosciences-discuss.net/5/2839/2008/ (Accessed 3 August 2016), 2008.
- 806 Shih, Y.-Y., Hung, C.-C., Gong, G.-C., Chung, W.-C., Wang, Y.-H., Lee, I.-H., Chen, K.-S. and Ho, C.-
807 Y.: Enhanced Particulate Organic Carbon Export at Eddy Edges in the Oligotrophic Western North



- 808 Pacific Ocean, *PLoS One*, 10(7), e0131538, doi:10.1371/journal.pone.0131538, 2015.
- 809 Shulzitski, K., Sponaugle, S., Hauff, M., Walter, K. D. and Cowen, R. K.: Encounter with mesoscale
810 eddies enhances survival to settlement in larval coral reef fishes, *Proc. Natl. Acad. Sci.*, 113(25), 6928–
811 6933, doi:10.1073/pnas.1601606113, 2016.
- 812 Siegel, D. A., Maritorena, S., Nelson, N. B. and Behrenfeld, M. J.: Independence and interdependencies
813 among global ocean color properties: Reassessing the bio-optical assumption, *J. Geophys. Res. C*
814 *Ocean.*, 110(7), 1–14, doi:10.1029/2004JC002527, 2005.
- 815 Siegel, D. A., Buesseler, K. O., Doney, S. C., Saille, S. F., Behrenfeld, M. J. and Boyd, P. W.: Global
816 Biogeochemical Cycles, *Global Biogeochem. Cycles*, 28, 181–196,
817 doi:10.1002/2013GB004743.Received, 2014.
- 818 Siegel, D. A. A., Court, D. B. B., Menzies, D. W. W., Peterson, P., Maritorena, S. and Nelson, N. B. B.:
819 Satellite and in situ observations of the bio-optical signatures of two mesoscale eddies in the Sargasso
820 Sea, *Deep. Res. Part II Top. Stud. Oceanogr.*, 55(10–13), 1218–1230, doi:10.1016/j.dsr2.2008.01.012,
821 2008.
- 822 Smeed, D.: Seasonal variation of the flow in the strait of Bab al Mandab, *Oceanol. Acta*, 20(6), 773–781
823 [online] Available from: /home/siccha/Documents/Library/Smeed 1997.pdf, 1997.
- 824 Smeed, D. A.: Exchange through the Bab el Mandab, *Deep Sea Res. Part II Top. Stud. Oceanogr.*,
825 51(4–5), 455–474, doi:10.1016/j.dsr2.2003.11.002, 2004.
- 826 Sofianos, S. S. and Johns, W. E.: An Oceanic General Circulation Model (OGCM) investigation of the
827 Red Sea circulation, 1. Exchange between the Red Sea and the Indian Ocean, *J. Geophys. Res.*,
828 107(C11), doi:10.1029/2001jc001184, 2002.
- 829 Sofianos, S. S. and Johns, W. E.: An Oceanic General Circulation Model (OGCM) investigation of the
830 Red Sea circulation: 2. Three-dimensional circulation in the Red Sea, *J. Geophys. Res.*, 108(C3),
831 doi:10.1029/2001jc001185, 2003.
- 832 Sofianos, S. S. and Johns, W. E.: Observations of the summer Red Sea circulation, *J. Geophys. Res.*
833 *Ocean.*, 112(6), 1–20, doi:10.1029/2006JC003886, 2007.
- 834 Sofianos, S. S., Johns, W. E. and Murray, S. P.: Heat and freshwater budgets in the Red Sea from direct
835 observations at Bab el Mandeb, *Deep Sea Res. Part II Top. Stud. Oceanogr.*, 49(7–8), 1323–1340,



- 836 doi:10.1016/S0967-0645(01)00164-3, 2002.
- 837 Sokal, R. R. and Rohlf, F. J.: Biometry; the principles and practice of statistics in biological research,
838 W.H. Freeman, San Francisco., 1969.
- 839 Souvermezoglou, E., Metzl, N. and Poisson, A.: Red Sea budgets of salinity, nutrients and carbon
840 calculated in the Strait of Bab-El-Mandab during the summer and winter seasons, *J. Mar. Res.*, 47(2),
841 441–456, doi:10.1357/002224089785076244, 1989.
- 842 Stramma, L., Bange, H. W., Czeschel, R., Lorenzo, A. and Frank, M.: On the role of mesoscale eddies
843 for the biological productivity and biogeochemistry in the eastern tropical Pacific Ocean off Peru,
844 *Biogeosciences*, 10(11), 7293–7306, doi:10.5194/bg-10-7293-2013, 2013.
- 845 Stukel, M. R., Aluwihare, L. I., Barbeau, K. A., Chekalyuk, A. M., Goericke, R., Miller, A. J., Ohman,
846 M. D., Ruacho, A., Song, H., Stephens, B. M. and Landry, M. R.: Mesoscale ocean fronts enhance
847 carbon export due to gravitational sinking and subduction, *Proc. Natl. Acad. Sci.*, 201609435,
848 doi:10.1073/pnas.1609435114, 2017.
- 849 Tiwari, S. P. and Shanmugam, P.: An optical model for deriving the spectral particulate backscattering
850 coefficients in oceanic waters, *Ocean Sci.*, 9(6), 987–1001, doi:10.5194/os-9-987-2013, 2013.
- 851 Tragou, E. and Garrett, C.: The shallow thermohaline circulation of the Red Sea, *Deep Sea Res. Part I*
852 *Oceanogr. Res. Pap.*, 44(8), 1355–1376, doi:10.1016/S0967-0637(97)00026-5, 1997.
- 853 Wafar, M., Qurban, M. A., Ashraf, M., Manikandan, K. P., Flandez, A. V. and Balala, A. C.: Patterns of
854 distribution of inorganic nutrients in Red Sea and their implications to primary production, *J. Mar.*
855 *Syst.*, 156, 86–98, doi:10.1016/j.jmarsys.2015.12.003, 2016.
- 856 Washburn, L., Kadko, D. C., Jones, B. H., Hayward, T., Kosro, P. M., Stanton, T. P., Ramp, S. and
857 Cowles, T.: Water Mass Subduction and the Transport of Phytoplankton in a Coastal Upwelling
858 System, *J. Geophys. Res.*, 96945(15), 927–14, doi:10.1029/91JC01145, 1991.
- 859 Xing, X. G., Claustre, H., Blain, S., D’Ortenzio, F., Antoine, D., Ras, J. and Guinet, C.: Quenching
860 correction for in vivo chlorophyll fluorescence acquired by autonomous platforms: A case study with
861 instrumented elephant seals in the Kerguelen region (Southern Ocean), *Limnol. Oceanogr.*, 10, 483–
862 495, doi:10.4319/lom.2012.10.483, 2012.
- 863 Yao, F., Hoteit, I., Pratt, L. J., Bower, A. S., Zhai, P., Köhl, A. and Gopalakrishnan, G.: Seasonal



- 864 overturning circulation in the Red Sea: 1. Model validation and summer circulation, *J. Geophys. Res.*
865 *Ocean.*, 119(4), 2238–2262, doi:10.1002/2013JC009004, 2014a.
- 866 Yao, F., Hoteit, I., Pratt, L. J., Bower, A. S., Köhl, A., Gopalakrishnan, G. and Rivas, D.: Seasonal
867 overturning circulation in the Red Sea: 2. Winter circulation, *J. Geophys. Res. Ocean.*, 119(4), 2263–
868 2289, doi:10.1002/2013JC009331, 2014b.
- 869 Zarokanellos, N. D., Papadopoulos, V. P., Sofianos, S. S. and Jones, B. H.: Physical and biological
870 characteristics of the winter-summer transition in the Central Red Sea, *J. Geophys. Res. Ocean.*,
871 120(11), 7237–7252, doi:10.1002/2017JC012882, 2017a.
- 872 Zarokanellos, N. D., Kürten, B., Churchill, J. H., Roder, C., Voolstra, C. R., Abualnaja, Y. and Jones, B.
873 H.: Physical Mechanisms Routing Nutrients in the Central Red Sea, *J. Geophys. Res. Ocean.*, 119(11),
874 8109–8121, doi:10.1002/2017JC013017, 2017b.
- 875 Zhai, P.: Buoyancy-driven circulation in the Red Sea, Massachusetts Institute of Technology and
876 Woods Hole Oceanographic Institution, Woods Hole, MA., 2014.
- 877 Zhan, P.: Sea Surface Height Variability and Eddy Statistical Properties in the Red Sea, , 1–66, 2013.
- 878 Zhan, P., Subramanian, A. C., Yao, F. and Hoteit, I.: Eddies in the Red Sea: A statistical and dynamical
879 study, *J. Geophys. Res. Ocean.*, 119(6), 3909–3925, doi:10.1002/2013JC009563, 2014.
- 880 Zhang, X., Hu, L. and He, M.-X.: Scattering by pure seawater: Effect of salinity, *Opt. Express*, 17(7),
881 5698–5710, doi:10.1364/OE.17.012685, 2009.
- 882



883 Table 1: Summary of measured parameters and associated sampling period for each glider mission

Seaglider Sensors	Dives	Deployment Period
C, T, P, BB3, FL3, O ₂	155	2-14 Dec 2014
C, T, P, BB3, FL3, O ₂	546	17 Dec 2014 – 2 Mar 2015

884

885 Table 2: Pearson correlations for air temperature and relative humidity versus mixed layer depth (MLD)

886 for four wind speed categories. Bold values indicate where $p < 0.05$, and where the correlation coefficient

887 $|r|$ is > 0.7 .

Wind Categories	Air temperature vs MLD		Relative humidity vs MLD	
	r	p	r	p
1) Wind Speed (0-7)	0.298	0.005	0.246	0.02
2) Wind speed (≤ 2)	0.375	0.152	0.325	0.219
3) Wind Speed (> 2 & ≤ 4)	0.301	0.019	0.294	0.022
4) Wind speed (> 4 & ≤ 7)	-0.084	0.805	-0.704	0.016

888

889 Table 3: Matrix with the loadings from the first two PCs. Bold number indicates the dominant

890 environmental parameters in each PC, indicated by the loadings with the highest absolute values. The

891 analysis of the winter period includes data for both glider missions, and for all fourth-depth ranges.

892

Both missions	The upper 200m		0-20 m		20-100 m		100-200 m	
	PC1	PC2	PC1	PC2	PC1	PC2	PC1	PC2
Temp	-0.41	-0.07	-0.58	-0.06	-0.48	-0.10	-0.43	-0.15
Sal	0.40	-0.13	0.48	-0.27	0.48	-0.20	0.42	0.19
Den	0.41	0.01	0.64	-0.03	0.53	0.00	0.44	0.19
Oxy	-0.37	-0.48	-0.14	-0.50	-0.28	-0.38	-0.41	-0.13
CHL	-0.35	0.41	0.00	0.54	-0.19	0.58	-0.35	0.21
CDOM	0.37	0.48	0.07	0.56	0.24	0.60	0.33	-0.05
bbp ₅₃₂	-0.33	0.59	0.01	0.27	-0.30	0.33	-0.21	0.92

893



894 Table 4: Pearson linear correlations between the atmospheric variables (air temperature, relative
 895 humidity and wind speed) versus mixed layer CHL, CDOM, bbp₅₃₂ and POC during the study period
 896 (both gliders missions). Where p-value is small ($p < 0.05$) then the correlation coefficient r is significant.
 897

Variables	Mean CHL in ML		Mean CDOM in ML		Mean bbp ₅₃₂ in ML		Mean POC in ML	
	r	p	r	p	r	p	r	p
Air temperature	-0.46	<0.01	-0.47	<0.01	0.18	<0.10	0.13	<0.21
Relative humidity	-0.41	<0.01	-0.34	<0.01	0.05	<0.66	0.01	<0.94
Wind speed	0.32	<0.01	0.30	<0.01	0.01	<0.94	0.02	<0.85

898

899

900 Table 5: Mean mixed layer CHL, CDOM, bbp₅₃₂, POC and POC:CHL ratio for latitudinal and
 901 longitudinal binned (0.03°) transect during the study period. Grey cells highlight the values that exceed
 902 50%.

	Date	CHL in ML	CDOM in ML	bbp ₅₃₂ in ML	POC in ML	POC:CHL in ML
M252-AB	AB-1: 2014/12/02-2014/12/08	0.10	0.65	$7.97 \cdot 10^{-4}$	14.91	287
	AB-2: 2014/12/08-2014/12/14	0.10	0.65	$8.16 \cdot 10^{-4}$	13.52	325
M250-ABC	ABC-1: 2014/12/17-2014/12/26	0.15	0.73	$8.10 \cdot 10^{-4}$	12.97	55
	ABC-2: 2015/01/03-2015/01/14	0.17	0.81	$7.58 \cdot 10^{-4}$	13.26	46
	ABC-3: 2015/01/14-2015/01/23	0.12	0.78	$7.80 \cdot 10^{-4}$	13.19	76
	ABC-4: 2015/02/04-2015/02/15	0.11	0.80	$9.36 \cdot 10^{-4}$	14.73	115
M250-CD	CD-1: 2014/12/26-2014/12/30	0.10	0.70	$8.11 \cdot 10^{-4}$	14.18	95
	CD-2: 2014/12/30-2015/01/03	0.13	0.75	$7.82 \cdot 10^{-4}$	13.87	60
	CD-3: 2015/01/23-	0.07	0.69	$9.14 \cdot 10^{-4}$	15.69	144



	2015/01/27					
	CD-4: 2015/01/28- 2015/02/04	0.07	0.75	$9.78 \cdot 10^{-4}$	17.48	157
Both missions	Mean	0.12	0.75	$8.77 \cdot 10^{-4}$	14.96	122
	STD	0.02	0.09	$1.29 \cdot 10^{-4}$	3.19	99

903

904

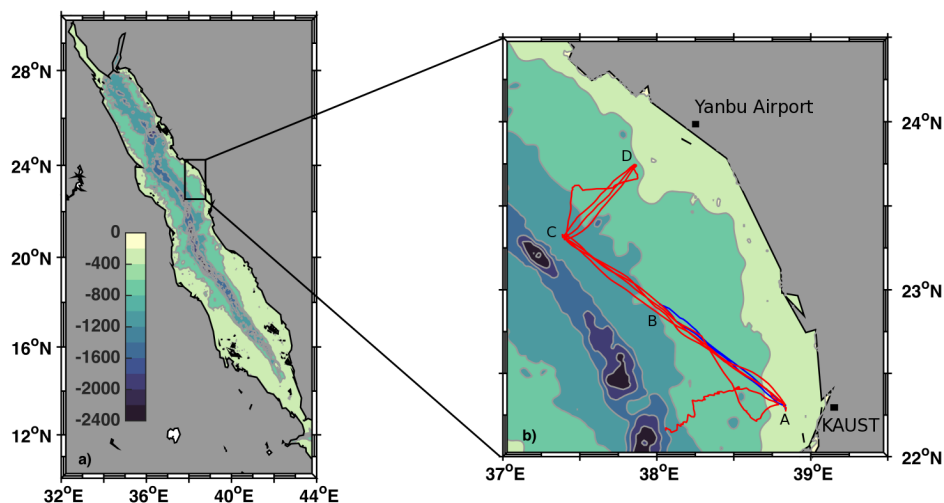


905

906

907 **Figures**

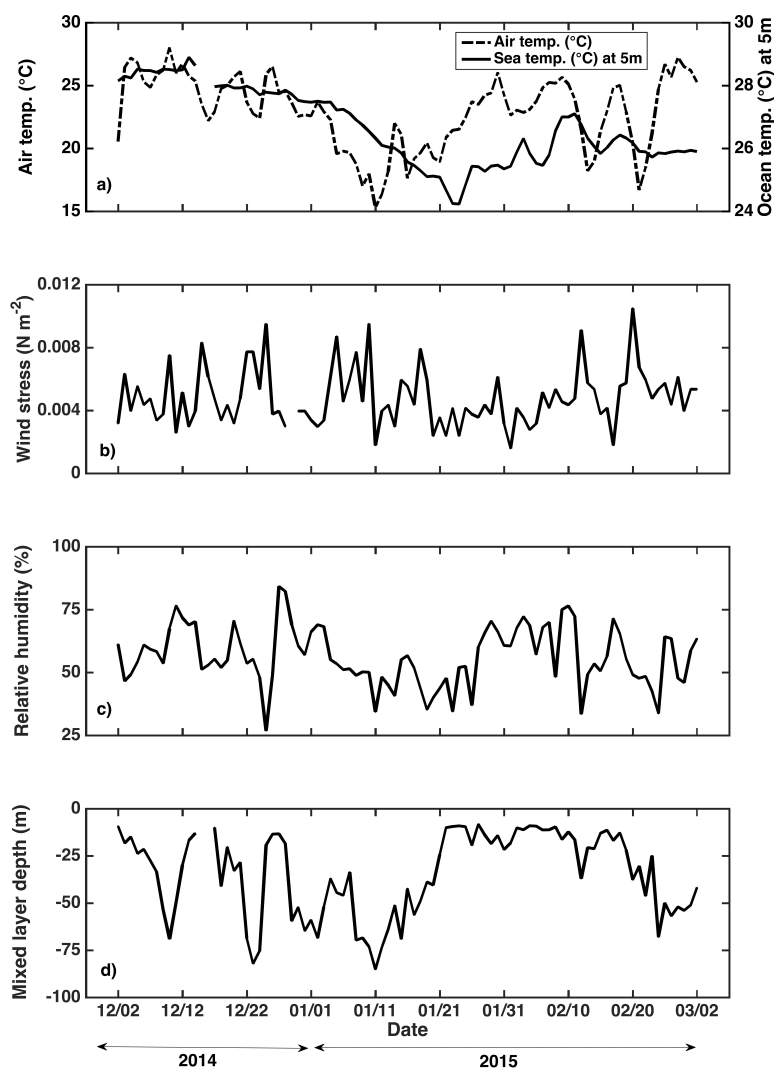
908



909

910 **Figure 1:** a) Bathymetric map of the Red Sea b) Bathymetric map of the study region with the two
911 glider missions. The blue line represents the glider mission that was conducted between 02/12/2014 to
912 14/12/2014 and the red line represent the glider mission from 17/12/2014 to 02/03/2015. The letters
913 A,B,C and D represent turning points of the glider missions segments.

914

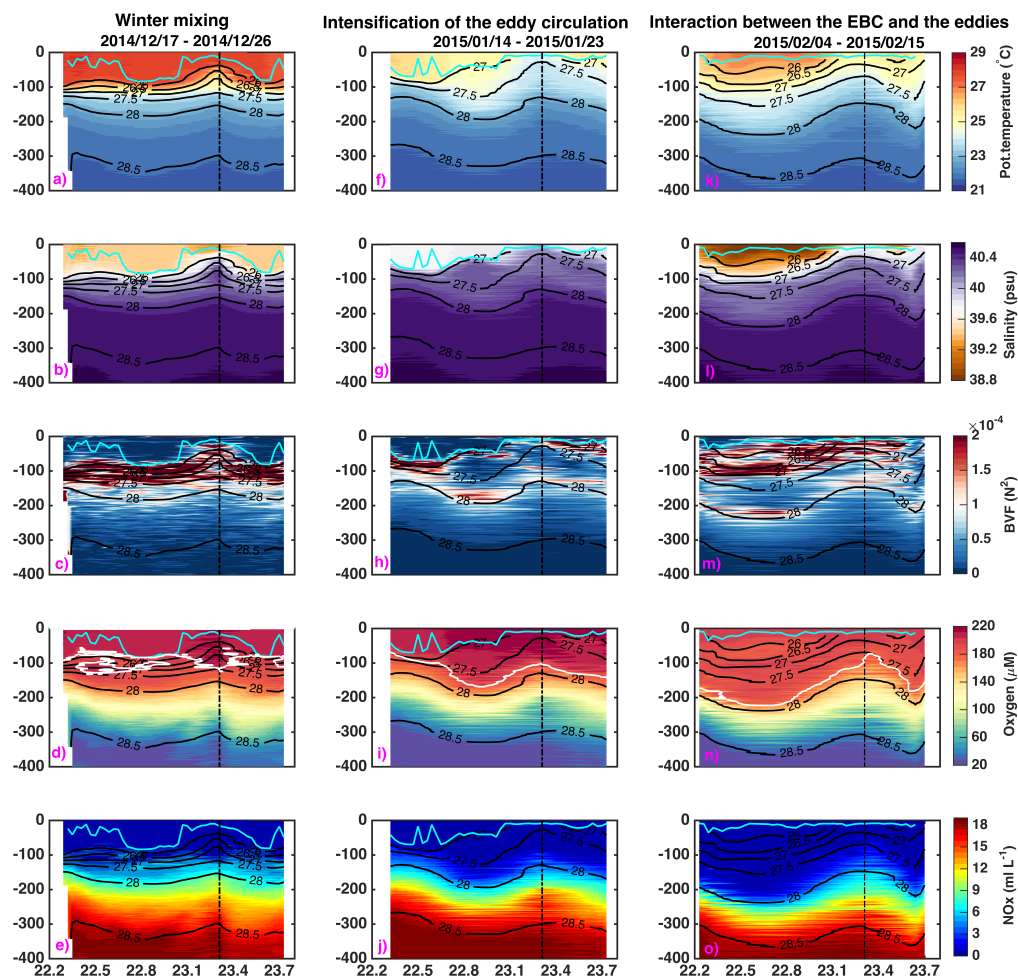


915

916 **Figure 2:** Daily mean of a) air temperature ($^{\circ}\text{C}$) b) wind stress (m s^{-1}) c) relative humidity (%) and
 917 Mixed Layer Depth (MLD) for the central Red Sea from December 2, 2014 to March 2, 2015.



918



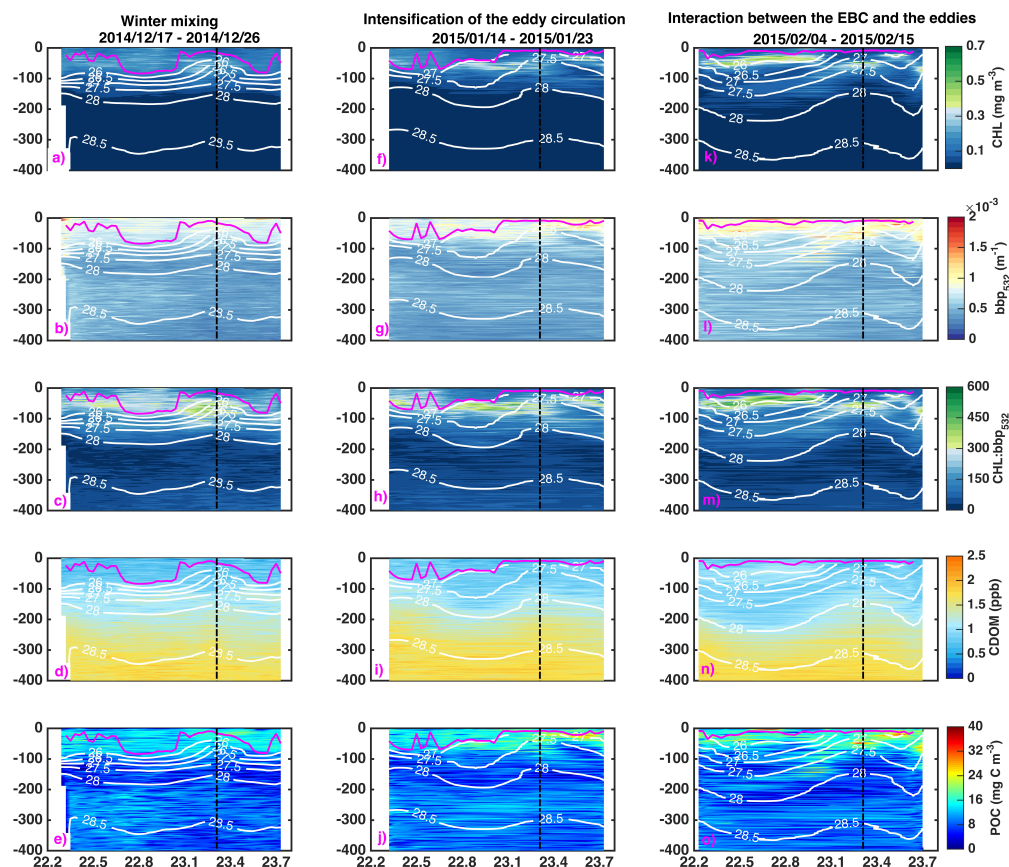
919

920

921 **Figure 3:** Seaglider sections plots for pot. temperature ($^{\circ}\text{C}$), salinity (psu), Brunt-Väisälä Frequency
 922 (BVF; N^2), oxygen (μM), and NO_x (ml L^{-1}) during the winter mixing period (a-e), the period of



923 intensification of the eddy circulation (f-j) and the interaction between the EBC/eddy interaction period
 924 (k-o). The vertical bold dash-dot black line indicates the turning point (C) as shown in Fig 1b.
 925 Isopycnals are indicated with a solid black line (contour interval = 0.5 kg m^{-3}). The magenta line
 926 represents the mixed layer depth (MLD) and the white line represents $180 \text{ } (\mu\text{M})$ isopleth.
 927



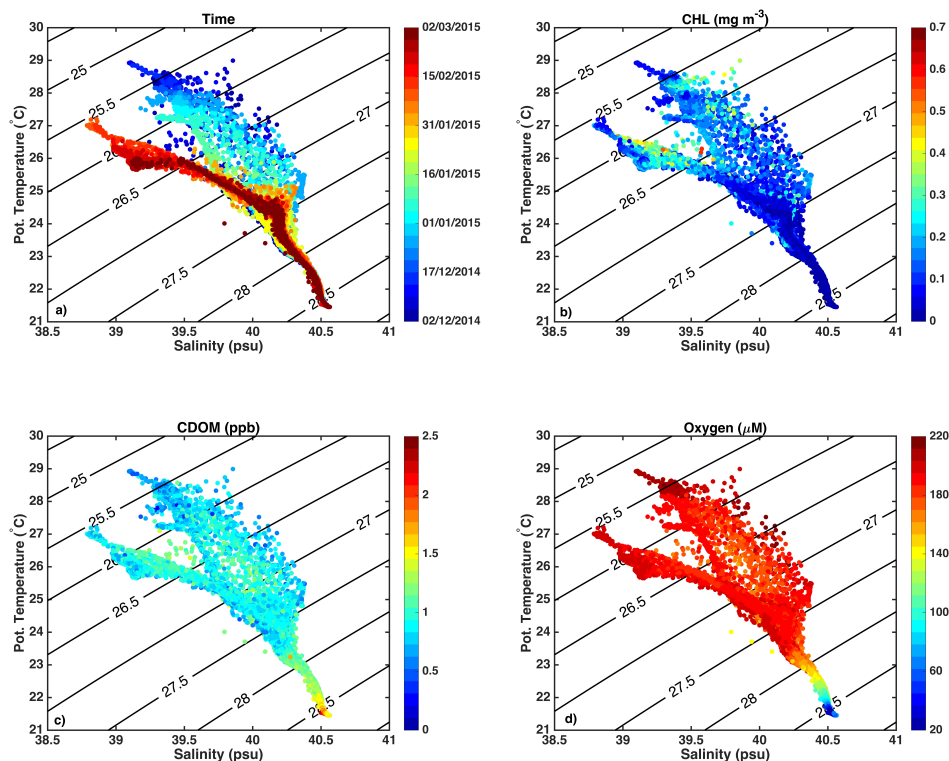
928

929 **Figure 4:** As in figure 3 but for CHL (mg m^{-3}), bbp_{532} (m^{-1}), $\text{CHL}:\text{bbp}_{532}$, CDOM, (ppb), POC (mg C m^{-3})

930 3), and NO_x (ml L^{-1}). Isopycnals are indicated with a solid white line (contour interval = 0.5 kg m^{-3}).



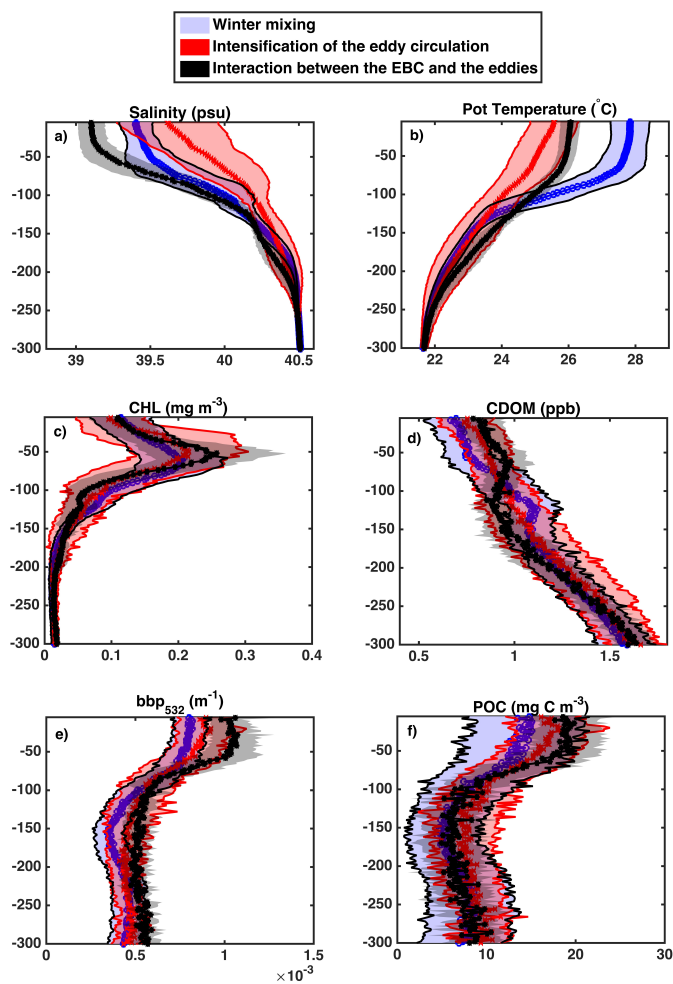
931



932

933 **Figure 5:** Pot. temperature–salinity diagrams from the two glider mission during the winter/early spring
934 period colored by a) date, b) CHL (mg m^{-3}), c) CDOM (ppb) and d) oxygen (μM).

935

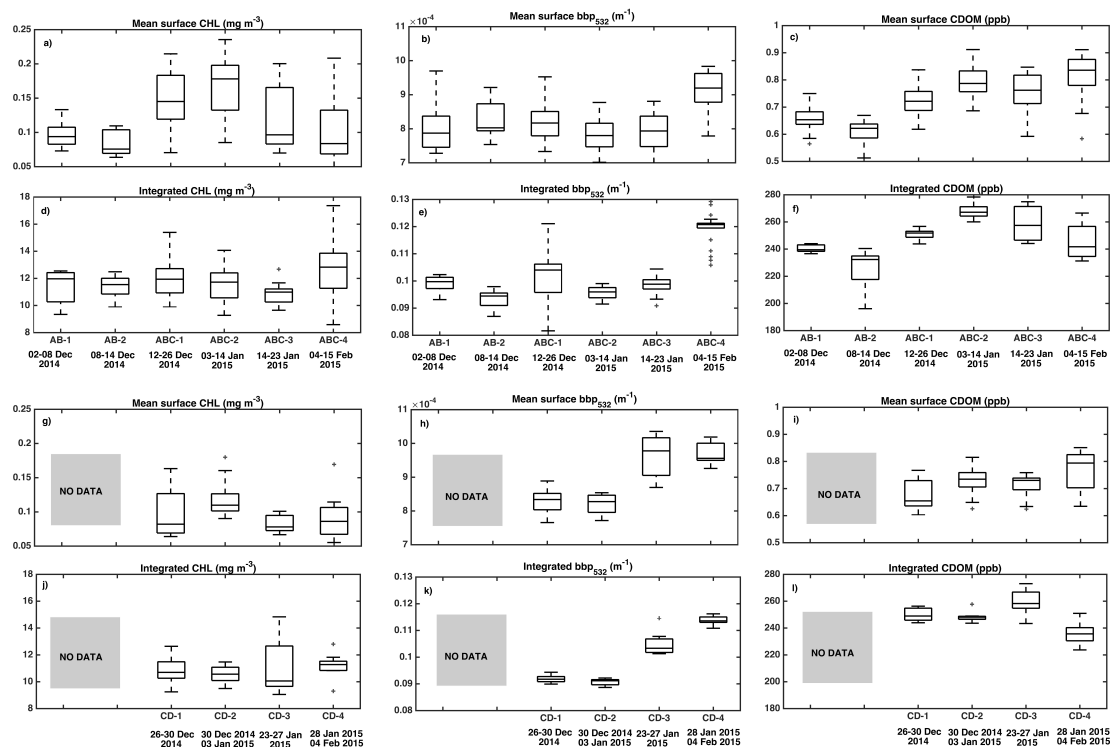


936

937 **Figure 6:** Mean vertical profiles of a) salinity (psu), b) pot. temperature (°C), c) CHL (mg m⁻³) d)
938 CDOM (ppb) e) bbp₅₃₂ (m⁻¹), and f) POC (mg C m⁻³) during the winter mixing (blue line), the
939 intensification of the eddy circulation (red line) and during the EBC /eddy interaction period (black
940 line). Shaded areas indicate the standard deviation for each period.

941

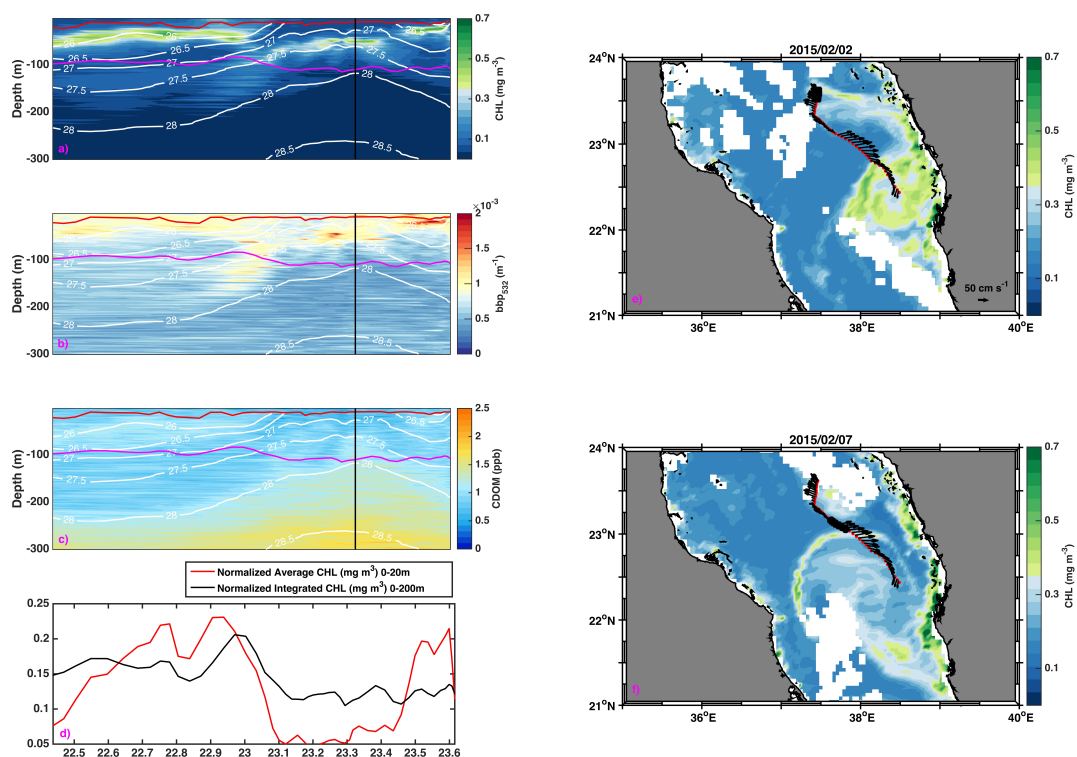
942



943

944 **Figure 7:** Box-and-whiskers plots for latitudinal (AB, AC) and longitudinal (CD) transects for the
 945 average 0-20m and integrated 0-200m for CHL (mg m^{-3}), bbp_{532} (m^{-1}), CDOM, (ppb) and POC (mg C
 946 m^{-3}) during the winter/spring period. The mean value of CHL, bbp_{532} , CDOM, and POC are shown with
 947 the range of variation as well the 25% and 75% quartiles.

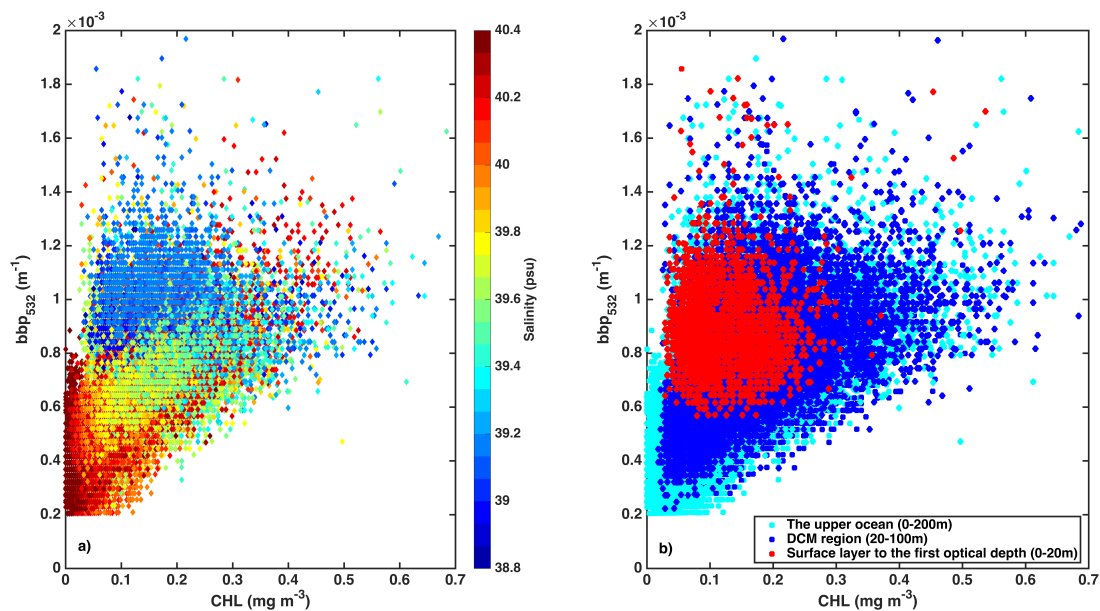
948



949

950 **Figure 8:** Snapshot of the front that developed during the EBC/eddy interaction. Seaglider section plots
 951 for a) CHL b) bbp_{532} and c) POC during the period of 2nd to 11th of February. Normalized 0-20m
 952 average CHL (red line) and 0-200m integrated CHL (black line). Daily MODIS-Aqua CHL for e) 2
 953 February 2015 and f) 7 February 2015. Red dots indicate the glider location and black vectors the glider
 954 derived surface velocity.

955



956

957 **Figure 9:** Scatterplot of a) $bbp_{532} (m^{-1})$ versus $CHL (mg m^{-3})$ where color indicates the salinity (psu). b)
958 $bbp_{532} (m^{-1})$ versus $CHL (mg m^{-3})$ in three depth categories: the upper ocean (0-200 m), DCM layer (20-
959 90 m) and the first optical depth (0-20 m).

960